

Model-Based Tissue Quantification from Simulated
Partial k-Space MRI Data

Model-Based Tissue Quantification from Simulated
Partial k-Space MRI Data

By

MEHRDAD MOZAFARI, B.Eng.,M.Sc.

A Thesis

Submitted to the School of Graduate Studies

in Partial Fulfillment of the Requirements

for the Degree

Master of Science

McMaster University

©Copyright by Mehrdad Mozafari, June 2008

MASTER OF SCIENCE(2008)
COMPUTING AND SOFTWARE

McMaster University
Hamilton, Ontario

TITLE: Model-Based Tissue Quantification from Simulated Partial k-Space
MRI Data

AUTHOR: Mehrdad Mozafari, M.Sc.

SUPERVISOR: Dr. Christopher Kumar Anand

NUMBER OF PAGES: xix, 111

Abstract

Pixel values in MR images are linear combinations of contributions from multiple tissue fractions. The tissue fractions can be recovered using the Moore-Penrose pseudo-inverse if the tissue parameters are known, or can be deduced using machine learning. Acquiring sufficiently many source images may be too time consuming for some applications. In this thesis, we show how tissue fractions can be recovered from partial k-space data, collected in a fraction of the time required for a full set of experiments. The key to reaching significant sample reductions is the use of regularization. As an additional benefit, regularizing the inverse problem for tissue fractions also reduces the sensitivity to measurement noise. Numerical simulations are presented showing the effectiveness of the method, showing three tissue types. Clinically, this corresponds to liver imaging, in which normal liver, fatty liver and blood would need to be included in a model, in order to get an accurate fatty liver ratio, because all three overlap in liver pixels (via partial voluming).

Acknowledgements

During the last two years I learned how to learn by my own, how to reflect my points of view and how to find myself better toward the road ahead in life. I learned how to better communicate with people and how to build relations and how to use my talents. I do owe all these to my supervisor Dr. Christopher Anand for his humble personality and kind behavior and I do appreciate his role in guiding me through my career and all his support for bringing this opportunity to me to fulfill my M.Sc. career.

I would like to thank my parents for being by my side. I wouldn't be able to do this without their support and encouragements. This is the least I can do to show my appreciation and thankfulness. My brother Ardavan and his wife Ayda and my little sister Golnaz were always supportive and I should thank them for their passion and kindness.

I would like to thank Dr. Jan Modersitzki and Dr. Mark Lawford for accepting to be committee members and for their helpful feedback on my thesis.

I had a wonderful time during the last two years, and I owe that to my wonderful friends Farhad, Kaveh, Hosein, Ershad, Rana, Zahra, Azin and Anis and so many more.

Contents

Abstract	iii
Acknowledgements	v
List of Figures	xi
List of Tables	xix
Preface	xxi
1 Basic MRI	1
1.1 Introduction	1
1.2 Medical Imaging	1
1.2.1 Magnetic Resonance Imaging (MRI)	3
1.2.2 Tomography	3
1.2.3 Ultrasound	4
1.2.4 MRI vs CT	4
1.3 Basic MRI	7
1.3.1 Resonance and Relaxation	9

1.3.2	Longitudinal Relaxation T_1	11
1.3.3	Transverse Relaxation T_2	12
1.4	MRI Scanner	14
1.4.1	Phase Encoding	16
1.4.2	Frequency Encoding	16
2	Segmentation	19
2.1	Introduction	19
2.1.1	Diagnostic Imaging	21
2.2	Image Segmentation Methods	22
2.2.1	Thresholding	22
2.2.2	Histogram-Based Methods	23
2.2.3	Deformable Models (Active Contours)	24
2.2.4	Clustering Methods	25
2.2.5	Region Growing Method	26
2.2.6	Artificial Neural Networks	28
2.2.7	Atlas-Guided/Model-Based Segmentation	28
3	k-Space	31
3.1	Introduction	31
3.1.1	What Is k-Space?	32
3.1.2	Conjugate Symmetry of k-Space Data	33
3.1.3	Data in k-Space	34
3.2	Full and Partial k-Space	38
3.2.1	Half Fourier Projection	39

3.2.2	Removing Lines	39
4	Tissue Quantification	43
4.1	Quantification Techniques	43
4.2	Tissue Quantification Using the Dixon Method	45
4.2.1	A Model for Tissue Quantification	45
4.3	Dixon Method	46
4.3.1	An Example	47
4.4	Specifying the Transformation S	48
5	Inverse Problems	51
5.1	Forward Problem	51
5.2	Inverse Problem	52
5.2.1	Linear Inverse Problem	53
5.2.2	Linear Least Squares	53
5.3	Modeling the Quantification Problem	54
5.3.1	Projection P	55
5.3.2	Fourier Transformation FT	58
5.3.3	Pixelwise S_p Transformation	59
5.3.4	Experimental Data b	60
5.3.5	Solver	61
5.3.6	Constraints	64
5.4	Regularization	64
5.5	Tikhonov Regularization	66
5.5.1	Choice of Regularization Operator R	67

5.5.2	Regularization Parameter	69
5.5.3	Determination of the Regularization Parameter via the L-curve Approach	71
6	Numerical Results	75
6.1	Geometrical Phantoms	75
6.2	Tissue Quantification	79
6.2.1	Full Sampling	81
6.2.2	Quantification From Partially Sampled Data (Without Regularization)	86
6.2.3	Partial k-Space Sampling with Noise Reconstructed Us- ing Regularization	92
6.2.4	L-curve	93
6.2.5	Standard Deviation of Noise	96
6.2.6	Execution Time	99
7	Conclusion and Future Work	101
7.1	Conclusion	101
7.2	Future Work	102
	Appendix	103

List of Figures

1.1	Multiple two-dimensional cross sections (slices) of the brain, starting from the right ear and ending at at the left ear. Derived from [39].	6
1.2	Spin direction is defined by a vector passing through the hydrogen atom.	8
1.3	RF pulse wobbles the equilibrium and make the magnetization vector M_Z spiral down toward the XY plane.	11
1.4	T_1 Relaxation of hydrogen atom with RF = 1.5T (Tesla) excitation.	12
1.5	T_2 Relaxation of hydrogen with RF = 1.5T (Tesla) excitation.	13
1.6	Image acquisition based on different relaxation times from the same anatomy result in different images. (a)Data acquisition using T_1 relaxation (b)Data acquisition using T_2 relaxation [30].	14
1.7	Using different gradients for phase encoding. Resolution increases with the number of phase-encoding steps [9].	17

2.1	Different approaches toward image segmentation. (a) shows an image with three items to be segmented, (b) is the segmentation by means of contours to show different constituents in one image together (c)-(d) shows the segmented items as a separate image.	20
2.2	Image segmentation using thresholding. (a) is the original image and (b) is the segmented image with two regions.	23
2.3	Segmentation by means of a growing contour.	25
2.4	k-means algorithm used for segmentation of randomly spread points [38] (a) choose 3 cluster center (b) shows the 3 clusters (c) choose a new center (d) set point to the corresponding cluster by minimizing the distance of each point to the center.	27
3.1	Image space and k-space [5] (a)Image space (b)k-space (c)Conjugate symmetry of k-space.	34
3.2	Different constituents of a sample MR signal from a MRI scanner (a)Constituents of read-out MR signal (b)MR signal containing information from all over the image.	35
3.3	Visualizing k-space by mapping amplitude of signal to each pixel value (a) Sampling the first row in k-space. (b) Building k-space row by row.	36
3.4	Location of certain information in k-space [17] (a)Full k-space with very detailed image (b) Low-pass filter, center of k-space contains low spatial frequencies signals and information of contrast in image (c) High-pass filter, borders of k-space contain high spatial frequencies and information of edges.	37

3.5	Presentation of image in both image-space and k-space (a)-(d)image-space (e)-(f) k-space.	38
3.6	Full vs half k-space	40
3.7	Different partial sampling of k-space causes aliasing and artifact in reconstructed image. The corresponding sampling of k-space is presented in Table 3.1.	41
4.1	Three simulated tissue fractions (ρ_1, ρ_2, ρ_3) shown in separate images.	48
4.2	Having the portion of each tissue in each voxel, we can find the density of each voxel in different experiment. Real and imaginary parts for one experiment for each tissue after applying the S transformation.	49
4.3	Linear combination of tissue using S . (a) Real part (b) Imaginary part	49
5.1	Structure of block-diagonal matrix P for e experiments.	56
5.2	A sample 5×5 block of P . (a)Sampling complex data (b)Sampling data with separated real and imaginary part.	57
5.3	Removing the singularity of matrix P by deleting rows with zeroes on the diagonal.	58
5.4	The product ($P \cdot FT$) is also a block-diagonal matrix.	59
5.5	Matrix S indicates the signal produced by pure tissue for different experiments where Exp_i represents different experiments and T_i represents different tissues.	60

5.6	Matrix S_p , having t different tissues and e MR experiments. $R_{t,m}$ is $a_{t,m}$ in the 2×1 block format shown in (5.6).	61
5.7	Pseudo-code for segmentation k columns at a time, where $P(n, k)$, <i>etc.</i> , set up the block matrices for images of size $n \times k$	64
5.8	<i>Col</i> matrix used to regularize image in column direction	68
5.9	<i>Col</i> matrix used to regularize image in column direction	69
5.10	Regularizing operator R consists of both row and column regu- larization.	70
5.11	The L-curve for standard form Tikhonov regularization [14]. The points marked by circles correspond to different regulariza- tion parameters, α	72
6.1	Geometrical phantoms representing different tissues in a target anatomy. An oblique cylinder, a box, and a sphere in one layer.	76
6.2	3D view of simulated tissues from different angles (a) top view (b)-(d) side view.	77
6.3	A 3D view of a layer of body, divided in to voxels. The structure of the top right voxel is shown separately, divided into subvoxels.	78
6.4	Simulated phantom representing flattened MR experiments shown in Figure 6.2.	79
6.5	Fully sampled experiments are simulated using the Bloch equa- tions from pure tissues as shown in Figure 6.4 using the S trans- formation. (a)-(d) is the real part and (e)-(h) is the imaginary part of the experiments, (i)-(k) is the quantified tissues from fully sampled MR experiments.	81

6.6 Fully sampled experiments contaminated by white Gaussian noise with low power $p = 0.1$ and its corresponding quantification. (a)-(d) is the real part and (e)-(h) is the imaginary part of the experiments. (i)-(k) is the segmented tissues from fully sampled noisy MR experiments. 83

6.7 Fully sampled experiments contaminated by stronger white Gaussian noise with higher power $p = 10$ and its corresponding quantification which, (a)-(d) is the real part and (e)-(h) is the imaginary part of the experiments, and (i)-(k) is the segmented tissues from fully sampled noisy MR experiments. 84

6.8 Fully sampled experiments contaminated by higher white Gaussian noise with higher power $p = 20$ and its corresponding quantification, which is not clear and contains lots of noises. (a)-(d) is the real part and (e)-(h) is the imaginary part of the experiments. (i)-(k) is the segmented tissues from fully sampled but very noisy MR experiments. 85

6.9 Segmented tissues from partially sampled non-noisy MR experiments with mapping shown in Table 6.2.2. The first two rows of the figure are the real and imaginary parts of the experiments, (a)-(c) are the segmented tissues from partial k-space. 58% of complete data was used. The results are without artifacts. . . 87

6.10 Segmented tissues from partially sampled non-noisy MR experiments with mapping shown in Table 6.4. The first two rows of the figure are the real and imaginary parts of the experiments, (a)-(c) is the segmented tissues form partial k-space. 48% of complete data was used.	88
6.11 Segmented tissues from partially sampled non-noisy MR experiments with mapping shown in Table 6.3. The first two rows of the figure are the real and imaginary parts of the experiments, (a)-(c) is the segmented tissues from partial k-space. 39% of complete data was used.	89
6.12 Segmented tissues from partially sampled noisy MR experiments with mapping shown in Table 6.4. The first two rows of the figure are the real and imaginary parts of the experiments, (a)-(c) is the segmented tissues from partial k-space. 48% of complete data was used. The results are still fine in spite of having noise.	90
6.13 Segmented tissues from partially sampled noisy MR experiments with mapping shown in Table 6.3. The first two rows of the figure are the real and imaginary parts of the experiments, (a)-(c) is the segmented tissues from partial k-space. 39% of complete data was used. Having noise and incomplete data, the segmentation result is full of noise and includes artifacts. We need to add a regularizer to change the problem.	91

6.14	Segmentation of partially sampled experiments. Using unweighted regularization ($\alpha = 1$) in both row and column direction improves the noise, especially in the background, removes the artifacts, and also adds a bit of smoothness to the segmented tissues. (a)-(c) are segmentation without regularization ($\alpha = 0$), (d)-(f) are the segmentation of the same tissue using unweighted ($\alpha = 1$) regularization.	93
6.15	Choosing very big or very small α causes over-smoothing and under-smoothing respectively. (a)-(c) are over-smoothed tissues, (d)-(f) are under-smoothed tissues.	94
6.16	L-curve (zoomed-in by using a linear-linear scale).	96
6.17	A comparison between different segmentations applied on the same partially sampled experiment with sampling patterns shown in 6.3 and with the same amount of noise. We obtained better segmentation results using weighted regularization. (a)-(c) is an unregularized segmentation($\alpha = 0$), (d)-(f) is the segmentation using unweighted regularization ($\alpha = 1$), (g)-(i) is the regularized tissue segmentation with regularization parameter ($\alpha = 3.5$). Only using 39% complete data used for image reconstruction. Table 6.2.4 shows the SNR of the segmented tissues.	97

List of Tables

3.1	Different partial sampling of k-space.	41
5.1	Solving the problem in a single step, rather than several columns at a time, results in very large matrix sizes in $\ Ax - b\ _2^2$	63
6.1	Sampling of rows from k-space of experiments shown in Figure 6.9.	87
6.2	Sampling of rows from k-space of experiments shown in Fig- ure 6.10.	88
6.3	Sampling of rows from k-space of experiments shown in Fig- ure 6.11.	89
6.4	Sampling of rows from k-space of experiments shown in Fig- ure 6.12.	90
6.5	Signal to Noise Ratio (SNR) related to segmented tissues shown in Figure 6.17 with the same order as tissues are presented. . .	98
6.6	Standard deviation of results of different problems.	98
6.7	Regularized segmentation. Execution time increases by increas- ing the size of the image.	99

Preface

In this thesis we show that the quantification of multiple tissues using multiple magnetic resonance images can be done from incomplete data, and that the quantitative and qualitative measures of the results can be improved by using regularization. Partial sampling of images saves scanning time dramatically (relative to conventional methods) but leads to artifacts and unwanted noise in the final segmented images. Considering the chemical property of tissues and the way tissue molecules respond in magnetic fields, we can model the problem as an inverse problem. In this thesis we describe the inverse problem in general, but focus on the reduction of sampling time. Numerical simulation shows that adding regularization to our inverse problem improves the results and enables us to remove errors and artifacts. Results show that by solving the regularized inverse problem, we can save up to 61% of scanning time and get acceptable segmented tissues.

The thesis contains seven chapters with three main topics, namely, the basics of MRI, MR k-space data and inverse problem modeling of the segmentation/quantification problem. We have attempted to make this thesis self-contained and accessible to be a general audience by giving a short intro-

duction to MRI in chapter 1, and try to explain the concepts that are needed to better understand our problem. Basic MRI introduces the concepts behind the problem as used in later chapters. In the second chapter, we present a critical appraisal of the current status of semiautomated and automated methods for the segmentation of anatomical medical images and also introduce terminology and important issues in image segmentation. In chapter 3, we talk about the MR readout signal and its properties in terms of k-space. The Dixon fat and water separation method is presented in chapter 4, and we extend this technique to separation of any arbitrary number of tissues. We introduce the modeled-based segmentation inverse problem in chapter 5 and go through details of each component of the problem and show how to use regularization to overcome the ill-posedness of the problem. Finally we report on numerical experiments with and without partial sampling, simulated noise, and regularization in chapter 6.

Chapter 1

Basic MRI

1.1 Introduction

In this chapter we will review the basic concepts of medical imaging with concentration on magnetic resonance imaging. Different image acquisition techniques and their applications are presented focusing on their applications. We will talk about physics principles of MRI, and finally we describe terminology and related concepts that are needed to understand our segmentation problem.

1.2 Medical Imaging

Medical imaging refers to the techniques and procedures used to visualize the inside of the human body for clinical purposes or medical science [41]. This process consists of various aspects such as:

- Computer processing, analysis and modeling
- Instrumentation and image acquisition
- Physics of image

Medical imaging is a rich source of mathematical inverse problems. From the effect (the observed image), the property of tissues can be inferred. For example, a 2D image of a body containing a cancerous tissue can be diagnosed by modeling the problem in comparison to a healthy tissue of the same anatomy.

The most common image acquisitions are:

- Fluoroscopy
- Magnetic Resonance Imaging (MRI)
- Nuclear Medicine
- Photoacoustic Imaging
- Projection Radiography
- Tomography
- Ultrasound

In the following sections, we will go through different image acquisition techniques, and discuss the advantages and disadvantages of each one. Finally, we will explain the fundamentals of the technique we chose for our image-segmentation problem, MRI, in detail and compare it with other imaging techniques.

1.2.1 Magnetic Resonance Imaging (MRI)

Magnetic resonance imaging uses the polarized and excited hydrogen nuclei (single proton) in water molecules in human tissue to produce a detectable signal which is spatially encoded, resulting in images of the body [11]. Three different kinds of electromagnetic fields are involved in the process of image acquisition:

1. a static magnetic field to polarize the hydrogen nuclei called B_0 ,
2. a radio frequency (RF) field for excitation of the hydrogen atoms to produce detectable signals, collected through an RF antenna,
3. a gradient field G varying linearly in space, used to specially encode the hydrogen atoms.

The strength of the three mentioned magnetic fields are

$$RF < G < B_0$$

Further details regarding magnetic resonance imaging are described in section 1.3.

1.2.2 Tomography

Tomos means “a section” or “a cutting” in Greek. Tomography is the method of imaging a single plane, or slice, of an object resulting in a tomogram. In tomography we usually gather projection data from multiple directions and feed

the data into a tomographic reconstruction software algorithm processed by a computer. Among the several forms of tomography, computed tomography (CT) is the most common technique.

CT or CAT scan is a noninvasive procedure that produces a 2D image of the structures in a thin slice of the body [6]. Ionizing x-ray beams are directed to the body, and collected and measured after passing through the body. The strength of the signals is inversely proportional to the absorption of different tissue and shows the density of corresponding tissues.

1.2.3 Ultrasound

Medical ultrasonography is a real-time scanning process that uses high-frequency sound waves between 2.0 to 10.0 MHz that are reflected (echo) by tissue with different mechanical properties to produce a 2D image. Ultrasound has several advantages which make it ideal for real-time application. Unlike CT, ultrasound is not harmful to the body. It is also relatively cheap and quick to perform. 3D ultrasound is a technique that can be used to visualize a three-dimensional view of the fetus during pregnancy [1]. However, the images are low quality compared to MRI or CT, and that limits the application of ultrasound imaging.

1.2.4 MRI vs CT

A computed tomography (CT) scanner is based on x-ray technology, using ionizing radiation during data acquisition. It performs reasonable scans on tissues composed of elements of a relatively higher atomic number than the

tissue surrounding them, such as bone and calcified tissues within body. This radiation can alter the chemical structure of cells and are harmful in general. As far as the human body is concerned, there are three systems which are affected by x-rays:

1. **Genitalia:** May have a negative effect on progeny.
2. **Skin:** Causes rash, hair loss and, apart from being cosmetically harmful, also predisposes to cancer.
3. **Blood:** Red and white blood cells exposed to x-rays may cause anaemia or disorders of the immune system.

On the other hand, MRI uses non-ionizing radio frequency (RF) signals for acquiring its images and is very well suited for non-calcified tissues. It is not harmful to the body and can reveal more detailed information about different tissues. Therefore, MRI is best suited for cases where a patient is to undergo the exam several times, as it avoids the hazard of ionizing radiation.

Both CT and MRI scanners are capable of generating multiple two-dimensional cross-sections (slices) of tissue and also three-dimensional reconstructions. Figure 1.1 on page 6 shows different slices of human brain in order to reconstruct a 3D model. One of the major differences between MRI and CT scans is that, unlike CT, we can set different parameters in MRI scans in order to get images with different contrasts. By changing scanning parameters, such as gradient fields and RF pulse, tissue contrast can be altered in various ways to point out different and more desired features. In section 1.4 we will talk more about the features and properties of a MRI scan and will show an

example of MRI scan with different gradient-field strength in Figure 1.7 on page 17.



Figure 1.1: Multiple two-dimensional cross sections (slices) of the brain, starting from the right ear and ending at at the left ear. Derived from [39].

Another advantage of an MRI scan is the capability of generating cross-sectional scans in any plane (including oblique planes). CT is limited to acquiring images in the axial (or near axial) plane. For purposes of tumor detection and identification, MRI is generally superior. However, CT usually is more widely available, faster, much less expensive, and easier for patients, unlike MRI, which takes a long scanning time and has a loud disturbing noise.

1.3 Basic MRI

The human body is largely made up of water and fat. Water is the major source of hydrogen in the body, followed by fat. Only considering these two elements, 63% of human body consists of hydrogen atoms. Because of the magnetic property of all hydrogen nuclei (protons) caused by a moving electric charge, they behave as small rotating magnets called nuclear spin. It means they generate an nuclear magnetic resonance (NMR) signal [24]. These electric charges spin very fast and produce a small, but noticeable magnetic field. The faster the spin speed, the larger the magnetic field. Each hydrogen atom can be considered as a tiny magnet, represented by a vector, passing through the center of the atom in order to define the spin direction. Figure 1.2 shows how to specify the spin direction. In MRI, the electron does not contribute to obtain a signal. However, there is different process for electron excitation similar to proton excitation called electron spin resonance. For further information you can refer to [28].

The magnetic vector of spinning protons can be decomposed into two

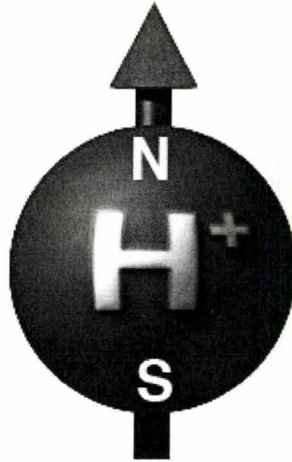


Figure 1.2: Spin direction is defined by a vector passing through the hydrogen atom.

orthogonal components: a longitudinal or Z component and a transverse component lying on the XY plane. In the absence of an external magnetic field, all hydrogen atoms are randomly ordered and the net magnetization vector, (NMV) or M_ϕ , that points to the Z direction is zero. When protons are exposed to a strong external magnetic field, B_0 , they tend to leave their current behavior and align with the direction of the magnetic field. After a while the spinning vector of all protons is either inline or in the opposite direction of B_0 with the same frequencies. In this case, the net magnetization vector, M_ϕ , is the sum of magnetization of all protons together in the Z direction. By applying this technique, a new criteria is introduced to keep track of any further changes in the behavior of protons. By considering the state of being aligned with B_0 as the initial state, any alteration, such as the frequency or

magnetization change, can be measured in comparison to the initial state.

1.3.1 Resonance and Relaxation

A new concept introduced here is called resonance. Resonance is the exchange of energy between two systems at a specific frequency. In the presence of B_0 , all the protons will settle to an equilibrium state. Magnetic resonance corresponds to the energetic interaction between spins and radio frequency electromagnetic waves.

The Larmor equation specifies the resonance frequency of each nucleus shown in equation (1.1), where γ is the gyromagnetic ratio, specific to each atom, between the external field and the resonance frequency, ω_ϕ is the angular frequency of precession of the nucleus in an external magnetic field, and B_0 is the strength of the external magnetic field. The stronger the B_0 , the higher the resonance frequency ω_ϕ .

$$\omega_\phi = \gamma B_0 \tag{1.1}$$

By applying a magnetic RF pulse on resonance, the protons can absorb extra energy, and tend to disarrange and start spinning in a different direction from B_0 . Only protons with resonant frequencies similar to the magnetic RF pulse will respond to that RF pulse.

The magnetic vector of spinning protons can be divided into two orthogonal components:

- A longitudinal component that goes along the \mathbf{Z} axis and is aligned with

B_0 .

- A transverse component, lying on the **XY** plane.

In the case of a pulse applied to a nucleus in the rest state, the initial magnetization vector M_Z that points along the Z direction (longitudinal) starts an spiral down toward XY plane shown in Figure 1.3. This modification in spin equilibrium and absorption of energy from the RF pulse is called excitation. During excitation time, longitudinal magnetization decreases and a transverse magnetization M_{XY} appears. It causes an asynchronization in spinning of protons in the direction of B_0 . On the other hand, there is relaxation time when the spinning proton returns from this state of imbalance to equilibrium. In the relaxation time, the electromagnetic energy gained from RF pulse is retransmitted. That is called the NMR signal¹. Relaxation combines two mechanisms:

- Longitudinal relaxation corresponds to magnetization recovery in the Z direction.
- Transverse relaxation corresponds to magnetization decay in the XY plane.

These relaxation times are called $T1$ and $T2$ and can be used to distinguish between different tissues, in the common case that they have different $T1$ and $T2$ values. In the following section, they are described in detail. We

¹Nuclei possesses an angular momentum called spin while being in the vicinity of an external magnetic field. The signal generated by nuclei spinning is called a NMR signal that can be calculated using the Larmor equation 1.1.

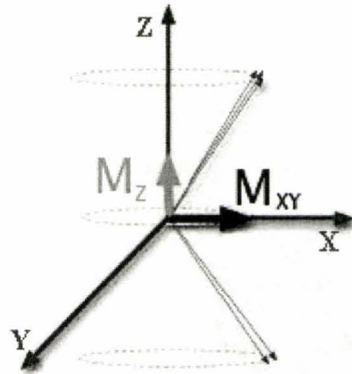


Figure 1.3: RF pulse wobbles the equilibrium and make the magnetization vector M_Z spiral down toward the XY plane.

consider an excitation with a 90-degree flip angle relative to the Z component of magnetization vector before the RF transmitter is turned off:

1.3.2 Longitudinal Relaxation T_1

Longitudinal or T_1 relaxation corresponds to the energy exchange between the spin and the lattice in the vicinity of the protons in order to re-establish the thermal equilibrium. When the transmitted RF pulse is stopped, the RF energy of the spinning proton is released back into the surrounding lattice. The recovery of longitudinal magnetization behaves as an exponential curve. T_1 is the time it takes during longitudinal relaxation to return to 63% of its final value (equilibrium state). The higher the strength of the main field, the longer T_1 . As an example, at 1.5 T (Tesla), T_1 values are approximately 200 to 3000 ms . The behavior of longitudinal relaxation is shown in equation (1.2).

Figure 1.4 shows the T_1 relaxation time in 63% of energy relaxation time

$$M_Z(t) = M_{Z,eq}(1 - e^{-\frac{t}{T_1}}) \quad (1.2)$$

where T_1 is the decay constant for recovery of the Z component of the nuclear spin magnetization, M_Z , and $M_{Z,eq}$ is the thermal equilibrium value.

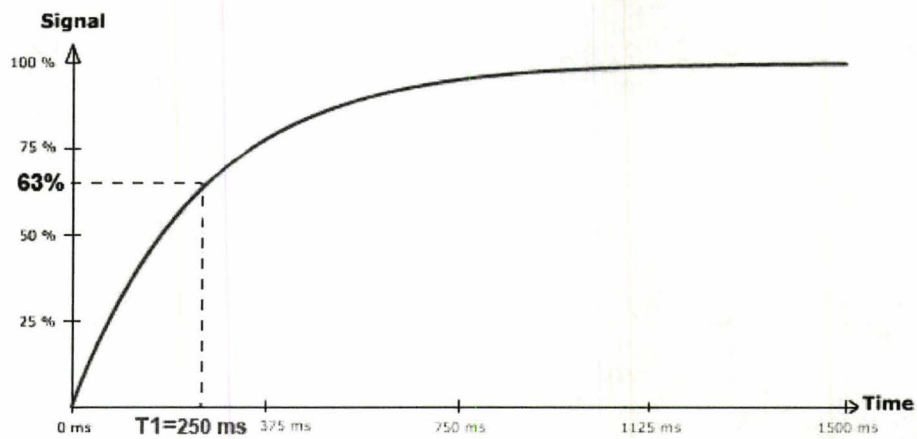


Figure 1.4: T_1 Relaxation of hydrogen atom with RF = 1.5T (Tesla) excitation.

1.3.3 Transverse Relaxation T_2

T_2 relaxation takes place in the transverse plane (XY plane). Also called spin-spin relaxation, it happens when spins are getting out of phase or switch between high and low energy state and exchange energy. If the energy is absorbed by the surrounding lattice, it results in the loss of transverse magnetization. Having different characteristics and different physical mechanisms makes T_1 and T_2 independent of each other.

The loss in phase causes decay in magnetization that can be shown as an exponential curve. T_2 is the time it takes transverse magnetization to lose 63% of its original value because it is the time constant of the first impulse response. It is the same as considering T_2 at 37% of its energy. The behavior of transverse relaxation is shown in equation (1.3)

$$M_{XY}(t) = M_{XY}(0)e^{-\frac{t}{T_2}} \quad (1.3)$$

where T_2 is the decay constant for the component of M perpendicular to B_0 and $M_{XY}(0)$ is the initial value of magnetization vector in the XY plane.

T_2 is tissue-specific and is always shorter than T_1 . Transverse relaxation is faster than longitudinal relaxation. The T_2 relaxation is temperature dependent. When the temperature is low it reduces the decay time and T_2 as well.

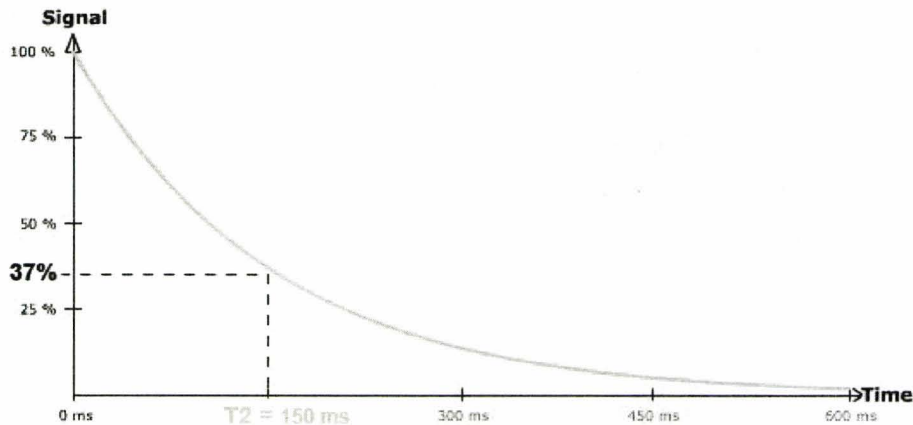


Figure 1.5: T_2 Relaxation of hydrogen with RF = 1.5T (Tesla) excitation.

The same anatomy appears differently depending on the scanning method

($T1$ or $T2$). Figure 1.6 shows two images from the same anatomy but acquired with two different relaxation times.

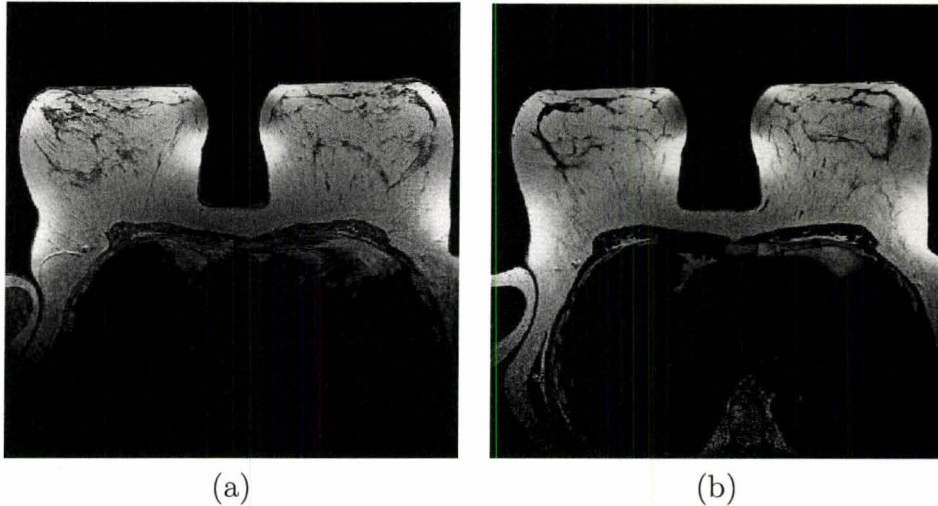


Figure 1.6: Image acquisition based on different relaxation times from the same anatomy result in different images. (a) Data acquisition using $T1$ relaxation (b) Data acquisition using $T2$ relaxation [30].

1.4 MRI Scanner

The MRI scanner can be used for cross-sectional views of the body. The output of the machine is different images from different layers of a particular anatomy.

The three major components of an MRI scanner are:

1. A static magnetic field
2. An RF transmitter and receiver
3. Three orthogonal, controllable magnetic gradients

While the patient lies in the MRI scanner, they are in a static magnetic field 10,000 to 30,000 times stronger than the magnetic field of earth. The external RF field causes excitation of hydrogen atoms. Tissues with less hydrogen atoms, such as bones, are darker while tissues with more hydrogen atoms, such as fat, are brighter in the final image, because of the stronger signals that result from the increased atom excitation.

The magnetic field B_0 is generated by either permanent magnets or electromagnets. There is a trade-off between the image quality and the strength of B_0 . Higher magnetic fields increase signal-to-noise ratio, permitting higher resolution or faster scanning [11]. However, higher field strengths require more costly magnets with higher maintenance costs, and have increased safety concerns². 1.0 – 1.5T field strengths are a good compromise between cost and performance for general medical use. However, for certain specialist uses (e.g., brain imaging), higher field strengths may be desirable (3T and higher).

The RF transmission is generated by a RF synthesizer, power amplifier and transmitting coil, and the receiver consists of the coil, preamplifier and signal-processing system [11]. Depending on the coil used here, data can be acquired in parallel which allows accelerated imaging. The most frequently used techniques are SENSE and GRAPPA. Sensitivity encoding (SENSE) is a technique that reduces MRI scan time considerably. The spatial information related to the coils of a receiver array are utilized for reducing conventional Fourier encoding [4]. In principle, SENSE can be applied to any imaging

²Because of the very strong magnetic field, the MRI suite can be a very dangerous place if strict precautions are not observed. Metal objects can become dangerous projectiles if they are taken into the scan room.

sequence and k-space trajectory. For further information about SENSE you can refer to [31].

Gradient coils are used to spatially encode the positions of protons. The gradient field causes the magnetic-field strength $B = B_0 + G$ to vary (increase or decrease) linearly across the imaging volume. These gradients are employed for slice selection, phase encoding and frequency encoding which are discussed in the following section. Scan speed is dependent on performance of the gradient system. Stronger gradients allow for faster imaging, or for higher resolution.

1.4.1 Phase Encoding

MR signals can be located by altering the phase of spins in one dimension with a pulsed magnetic-field gradient along that dimension prior to the acquisition of the signal. Images reconstructed at various levels of phase encoding show image sharpness to improve as the number of phase-encoding steps increases [9]. However, there is a trade-off between scanning time and the phase-encoding process. Figure 1.7 shows the steps during phase encoding.

1.4.2 Frequency Encoding

Reading out a signal in the presence of a constant gradient is called frequency encoding. It is a static gradient field which is necessary to acquire a set of signals with different frequencies in order to reconstruct the distribution of the sources along the direction of gradient field. We can use the Fourier transform to separate these signals.

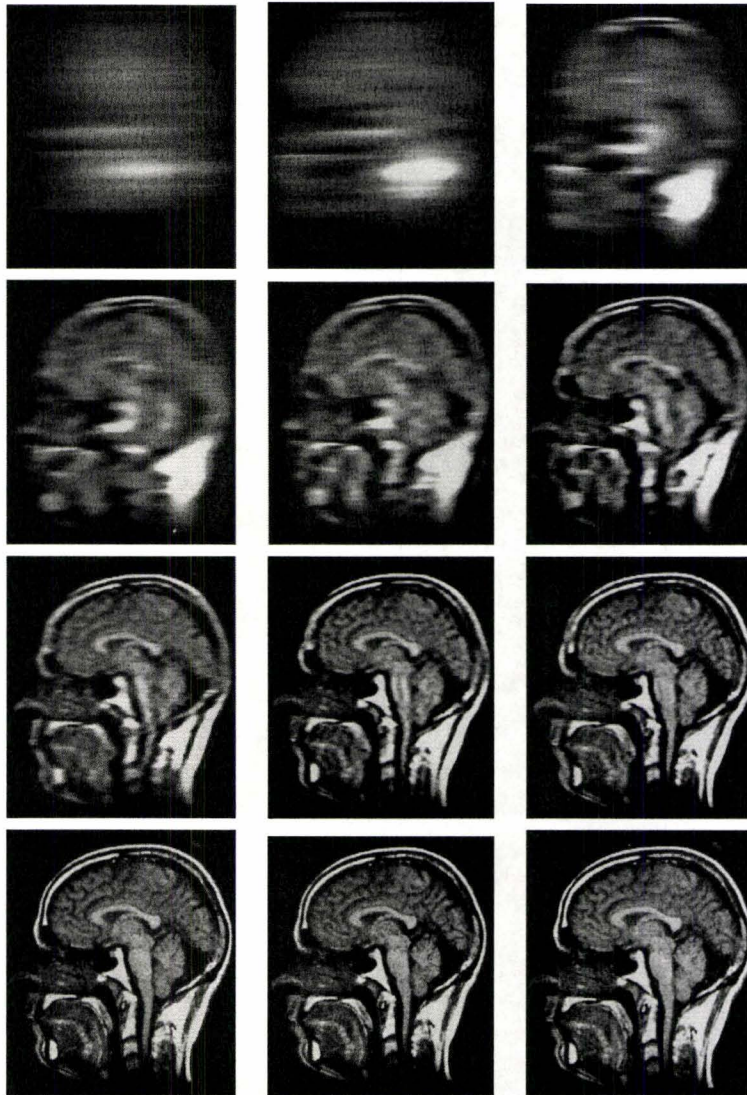


Figure 1.7: Using different gradients for phase encoding. Resolution increases with the number of phase-encoding steps [9].

Chapter 2

Segmentation

In this chapter we talk about different common segmentation techniques, commenting on their advantages and disadvantages. We also review basic terminology and important issues regarding segmentation and then present the quantification technique we are using in our optimization problem. Quantification gives more information about tissue composition than segmentation. Its potential applications in MRI are a superset of the applications of segmentation.

2.1 Introduction

In order to segment different objects and shapes in an image, the image needs to be parsed and analyzed by different algorithms. These algorithms that delineate anatomical structures and patterns in an image are known as segmentation techniques. Segmentation is the process of partitioning a digital image into its constituent parts that have similar characteristics or proper-

ties, such as texture, intensity or color [29]. In general there are two types of segmentation:

1. An image can be split to multiple images, each containing a certain constituent.
2. Contours can be used to indicate different constituents in one image.

We use the first approach in our segmentation problem, identifying tissue fraction in voxels containing multiple tissues. Figure 2.1 shows the two approaches.

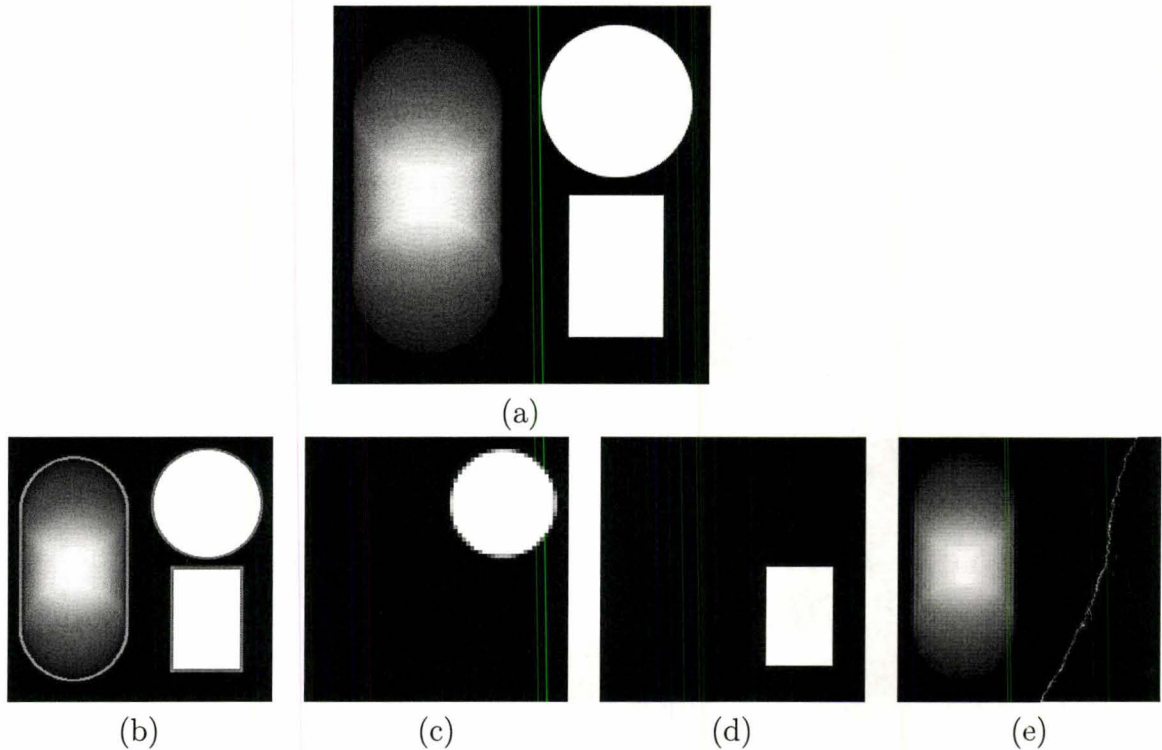


Figure 2.1: Different approaches toward image segmentation. (a) shows an image with three items to be segmented, (b) is the segmentation by means of contours to show different constituents in one image together (c)-(d) shows the segmented items as a separate image.

2.1.1 Diagnostic Imaging

Diagnostic imaging is an invaluable tool in medicine. MRI, CT, digital mammography, and other imaging modalities provide an effective means for acquiring the subject's anatomy [29]. These technologies have greatly increased knowledge of normal and diseased anatomy for medical research, and are critical components in diagnosis and treatment planning. Segmentation algorithms play an important role in many biomedical imaging applications such as:

- Computer-guided surgery
- Diagnosis
- Localization of tumors and other pathologies
- Quantification of tissue volume
- Study of anatomical structure
- Treatment planning

Or in different field of studies such as:

- Automatic traffic-controlling systems
- Face recognition
- Fingerprint recognition
- Locating objects in satellite images (roads, forests, etc.)
- Machine vision

However, the amount of the acquired data in both CT and MRI is very large (multiple images of the same anatomy), and it often takes physicians a lot of time to compare and analyze images correctly. Therefore, segmentation algorithms are intended to identify regions of interest in the images. In the following section, we describe a few techniques used for image segmentation.

2.2 Image Segmentation Methods

There are now a wide variety of image segmentation techniques, some considered general purpose and some designed for specific classes of images. Several general-purpose algorithms and techniques have been developed for image segmentation. Different segmentation algorithms might find different solutions. In some problems, these techniques often have to be combined with domain knowledge in order to effectively solve the problem. In the following section, we will describe various segmentation techniques.

2.2.1 Thresholding

The thresholding technique segments images by creating two partitions based upon the image intensities [33]. It is also called histogram-based model-image segmentation. The most important job is to choose an intensity value, called the threshold, which separates the desired classes. The segmentation is then achieved by grouping all pixels with intensities greater than the threshold into one class and all other pixels into another class.

Thresholding is often used as an initial step in the sequence of image

processing operation. One application of thresholding is tumor detection in mammography which is done by dividing tissues into two classes, considered as healthy and cancerous. An example of image segmentation by means of thresholding is shown in Figure 2.2.

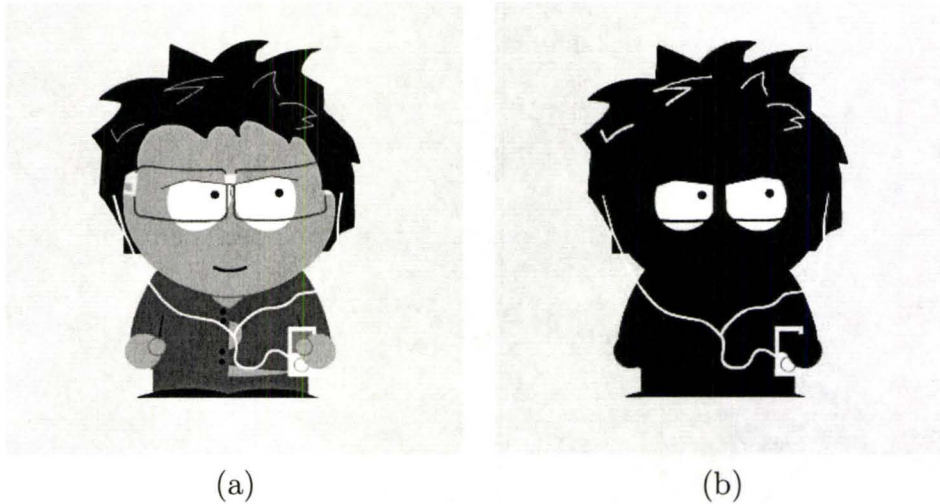


Figure 2.2: Image segmentation using thresholding. (a) is the original image and (b) is the segmented image with two regions.

The main drawback is that, in its simplest form, only two classes are generated, and it cannot be applied to multichannel images. In addition, thresholding typically does not take into account the spatial characteristics of an image. This causes the segmented images to be very sensitive to noise, which can occur in MR images [22].

2.2.2 Histogram-Based Methods

A simple improvement is introduced in thresholding called histogram-based segmentation. It separates the different parts of an image by thresholding

the histogram. It assumes that an image is composed of regions with different gray levels, and separates it into a number of peaks, each corresponding to one region. With this technique, segmentation is done using only one pass through the pixels [10]. A histogram is computed using all pixel values and then for each individual pixel, the peaks and valleys in the histogram are used to assign the pixel to a cluster. Histograms are based on different measurements, such as color or intensity. One of the disadvantages of the histogram-based segmentation is the difficulty in identifying significant peaks and valleys in the image.

2.2.3 Deformable Models (Active Contours)

This technique, also known as active contours or snakes, tries to delineate region boundaries by using closed parametric curves or surfaces that deform under the influence of internal and external forces. The first step in segmentation is to manually place a closed curve near the desired boundary and apply an iterative relaxation process [29]. The task is to minimize the force associated with the current contour as a sum of an internal and external force [18]. Internal forces are computed from within the curve to keep it smooth throughout the deformation. External forces are usually derived from the image to drive the curve or surface toward the desired feature of interest. Figure 2.3 shows the steps of segmentation using a contour which initiated from a circle, and deforms and grows until it reaches the boundary of the region of interest.

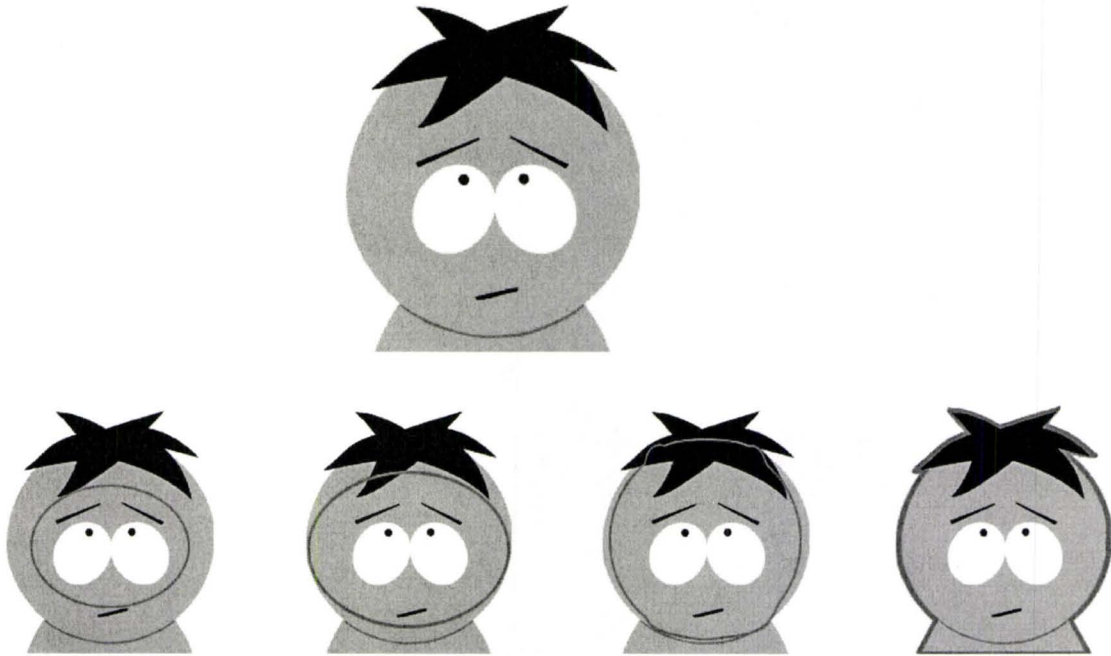


Figure 2.3: Segmentation by means of a growing contour.

2.2.4 Clustering Methods

Clustering methods are based on the concept of clustering algorithms such as the k-means algorithm, the fuzzy c-means algorithm and the expectation-maximization (EM) algorithm. The most commonly used algorithm is the k-means algorithm. It clusters n objects, based on certain attributes, into k partitions where $k < n$ [16]. The segmentation is done iteratively and starts by partitioning an image into k clusters and computing the mean intensity for each class. The basic algorithm is:

1. Use a heuristic function to pick k cluster centers.

2. Assign each pixel in the image to the cluster that minimizes the distance between the pixel and the cluster center.
3. Recompute the cluster centers by averaging all of the pixels in the cluster.
4. Repeat steps 2 and 3 until convergence is attained.

The distance can be defined as either a squared or absolute difference between each pixel value within the cluster and a cluster center, possibly including differences in intensity, pixel color, texture, and location, or a weighted combination of these factors. k can be selected manually, randomly, or by a heuristic. The quality of the solution depends on the initial set of clusters and the value of k . Figure 2.4 shows how the k-means algorithm segments objects by minimizing the squared error function.

2.2.5 Region Growing Method

Region growing is a technique for extracting a region in an image that is defined based on some certain criteria such as intensity information or edges in the image [15]. It takes a manually selected seed point as an input along with the image and extracts all pixels connected to the initial seed based on some predefined criteria during iterative steps. The difference between a pixel's intensity value and the region's mean, δ , is used as a measure of similarity. The pixel with the smallest difference measured this way is allocated to the respective region. This process continues until all pixels are allocated to a region.

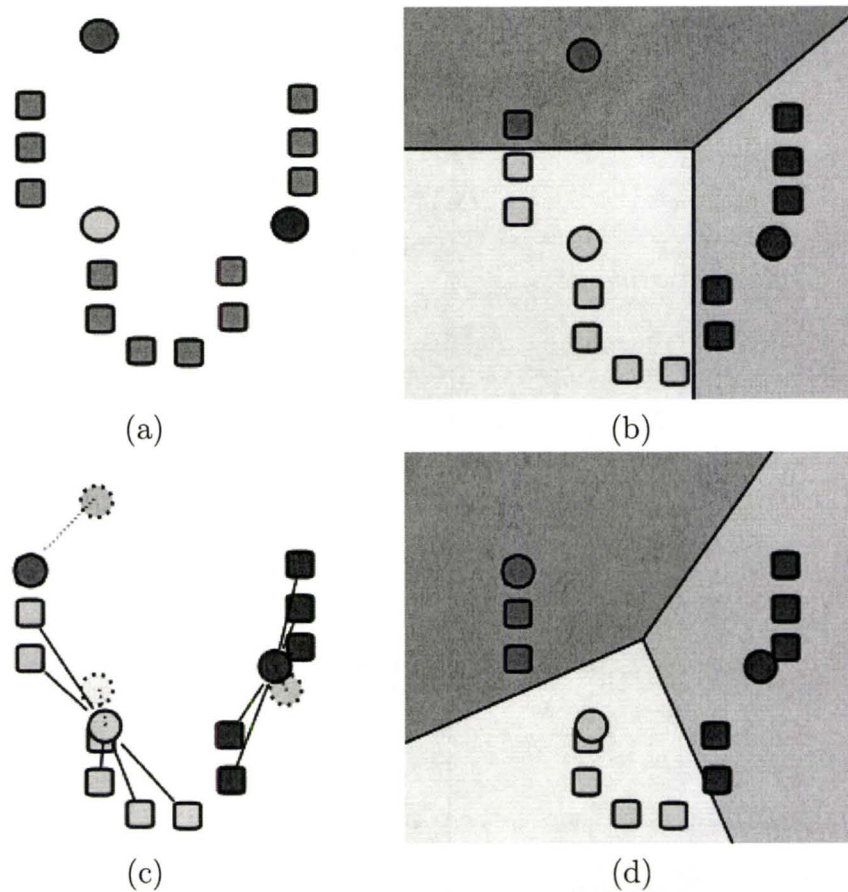


Figure 2.4: k-means algorithm used for segmentation of randomly spread points [38] (a) choose 3 cluster center (b) shows the 3 clusters (c) choose a new center (d) set point to the corresponding cluster by minimizing the distance of each point to the center.

The region growing method is typically used for the delineation of small, simple structures such as tumors and lesions. The primary disadvantage of region growing is that it requires manual interaction to obtain the seed point. Thus, for each region that needs to be extracted, a seed must be planted. Region growing can also be sensitive to noise, causing extracted regions to

have holes or even become disconnected [29].

2.2.6 Artificial Neural Networks

Artificial neural networks (ANNs) are parallel-network nodes that simulate biological learning. Each node is capable of performing elementary computations. Learning is achieved through the adaptation of weights assigned to the connections between nodes [7]. ANNs represent a paradigm for machine learning and can be used in a variety of ways for image segmentation.

2.2.7 Atlas-Guided/Model-Based Segmentation

Atlas-guided approaches are powerful tools for medical image segmentation when a standard atlas or template is available. The primary assumption of such an approach is that structures of interest/organs have a repetitive form of geometry called an atlas. The atlas is generated by compiling information on the anatomy that requires segmenting [29]. This atlas is then used as a reference frame for segmenting new images. The atlas introduces constraints which favor a certain shape.

Atlas-guided segmentation can also be considered as an image-registration problem. Image registration is the process of transforming the different sets of data into one coordinate system. Registration is necessary in order to be able to compare or integrate the data obtained from different measurements [43]. Such a task involves:

1. Registration of the training examples to a common pose by means of a

transformation (called atlas warping).

2. Probabilistic representation of the variation of the registered samples.
3. Statistical inference between the atlas and the image.

Chapter 3

k-Space

In this chapter we present the technique used for data acquisition from magnetic resonance (MR) signals. For 2D imaging, k-space can be thought of as a 2D complex matrix that stores the acquired MR data organized by the phase and frequency content. We will explain the different properties of k-space and how to move between k-space and image space using Fourier transformations. Then we will present how undersampling of the k-space helps us improve data-acquisition time, discussing the trade-off between undersampling and image quality in detail.

3.1 Introduction

In this section we will talk about the concept of k-space and the Fourier transform. We will also show a sample MR signal and its constituents.

3.1.1 What Is k-Space?

The task of an MRI scanner is to recognize and collect MR signals and store them in a specific order which is recognizable for further analysis. At each RF excitation, a combination of different excitations are collected as one complex signal as shown in Figure 3.2 on page 35. The read-out MR signal is stored in a 2D array called k-space, containing samples of the continuous Fourier transform of the object's magnetization.

In MRI theory [27], we can derive the equation for MR signals as

$$S(t) = \int_x \int_y m(x, y) e^{-i2\pi[k_x(t)x + k_y(t)y]} dx dy, \quad (3.1)$$

where

$$k_x(t) = \frac{\gamma}{2\pi} \int_0^t G_x(\tau) d\tau, \quad k_y(t) = \frac{\gamma}{2\pi} \int_0^t G_y(\tau) d\tau, \quad (3.2)$$

$m(x, y)$ is the transverse nuclear magnetization, and G_x, G_y are gradient fields in the x and y directions respectively [32]. Comparing the signal equation (3.1) with the Fourier transform of $m(x, y)$,

$$M(k_x, k_y) = \int_x \int_y m(x, y) e^{-i2\pi[k_x x + k_y y]} dx dy, \quad (3.3)$$

we can see that

$$s(t) = M(k_x, k_y), \quad (3.4)$$

or

$$s(t) = M\left(\frac{\gamma}{2\pi} \int_0^t G_x(\tau) d\tau, \frac{\gamma}{2\pi} \int_0^t G_y(\tau) d\tau\right). \quad (3.5)$$

Thus, k_x and k_y are in units of spatial frequency, typically cycles/cm. This is the most important relationship in MRI. At any given time t , $s(t)$ equals the value of the 2D Fourier transform of $m(x, y)$ at some spatial frequency. The total recorded signals $s(t)$ therefore maps directly to a trajectory through the spatial-frequency (Fourier transform) space as determined by the time integrals of the applied gradient waveforms $G_x(t)$ and $G_y(t)$. In the MR literature [25] and [37], the Fourier-transform space is often called k-space, where k represents the spatial-frequency variable. To form an image, the trajectories given by $s(t)$ should cover a sufficient part of the k-space to allow reconstruction of $m(x, y)$.

The relation/transformation between k-space data and image space is the Fourier transform. The Fourier transform of complete data, *e.g.* the Fast (Uniform) Fourier Transform, is an invertible transformation, and no data loss happens during each step of transformation.

$$\text{k-space} \xleftarrow{\text{fft2D}} \text{image-space} \xrightarrow{\text{ifft2D}} \text{k-space} \quad (3.6)$$

3.1.2 Conjugate Symmetry of k-Space Data

One of the most important properties of k-space that helps us reduce scanning time and reconstruct image is the conjugate symmetry of data. The entries in k-space are complex numbers that distinguish between signals with similar frequency but different phases. Figure 3.1 shows the conjugate symmetry of data in k-space.

Considering the conjugate symmetry of data, the full k-space information is redundant, and an image can be reconstructed using only part of

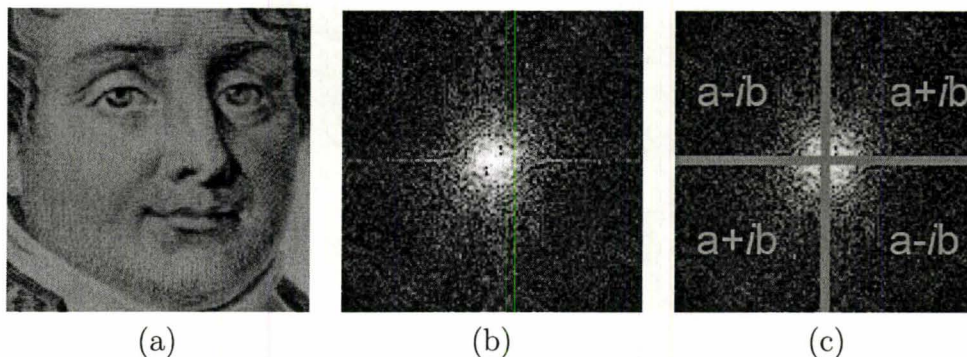


Figure 3.1: Image space and k-space [5] (a)Image space (b)k-space (c)Conjugate symmetry of k-space.

k-space. However, the MRI scanner is a very noisy environment and reconstructing the entire image using only a quarter of k-space data may result in a noisy and erroneous image. Different techniques such as Half Scan or Partial Fourier [20] scan can save a lot time during phase encoding. On the other hand, techniques such as half echo allow lower frequency-sampling rates and/or shorter echo times during frequency encoding.

3.1.3 Data in k-Space

The read-out signal is a mixture of different MR signals caused by spinning nuclei with different frequencies from all over the object being imaged. Figure 3.2 shows how different signals can combine together and build a complex signal.

By means of the Fourier transform, the constituent parts of each MR signal can be decomposed into a sum of sine waves of different frequencies,

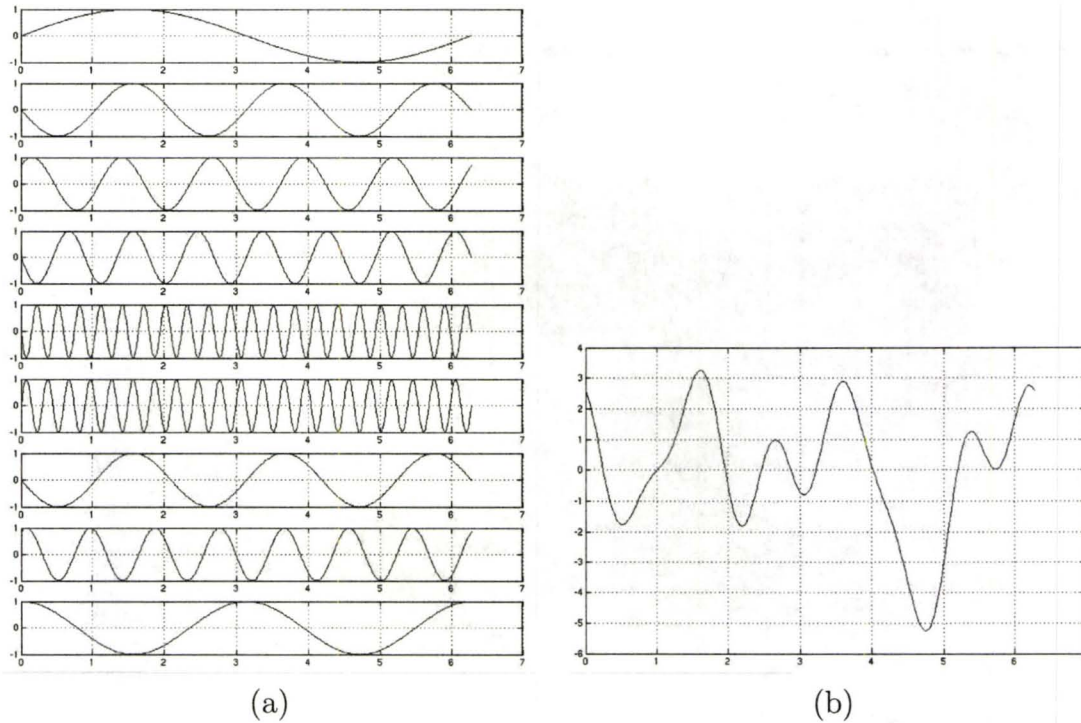


Figure 3.2: Different constituents of a sample MR signal from a MRI scanner (a)Constituents of read-out MR signal (b)MR signal containing information from all over the image.

phases and amplitude. Knowing frequency, amplitude and phase of each sine wave, it is possible to reconstruct the signal (inverse Fourier transform). The Fourier transform can tell us what these signals are with their exact frequency and amplitude. The challenge is to find the amplitude of the read-out signal at a certain voxel and translate it to a grayscale value in order to visualize the output image. By mapping the different amplitudes to a pixel value, k-space can be presented as an image. The higher the amplitude, the brighter the pixel shows up in k-space and vice versa. Figure 3.3 shows how each row in

k-space is acquired. By applying the proposed technique n times for an $n \times n$ image, we obtain a complex $2D$ matrix used for visualizing k-space.

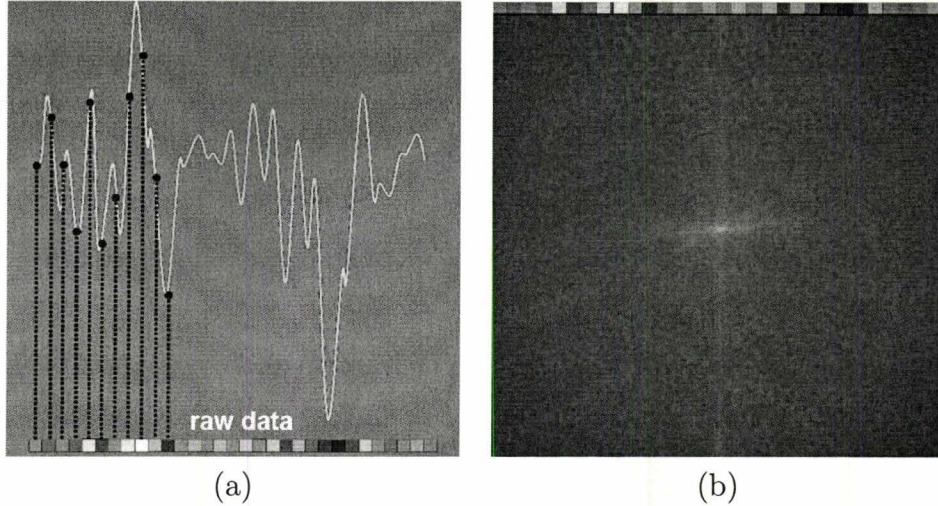


Figure 3.3: Visualizing k-space by mapping amplitude of signal to each pixel value (a) Sampling the first row in k-space. (b) Building k-space row by row.

The location of the data in k-space depends on the strength and the duration of the gradient field [36]. The higher the strength of the gradient, the faster the sampling position moves in k-space. The center of k-space¹ contains information of low spatial frequency. These signals have low frequencies and high magnitude. That is why the center of k-space is always brighter than the sides of k-space. On the other hand, the sides of k-space contain information of high spatial frequency. By applying a low-pass filter and high-pass filter, we can better show the role of each kind of signal in the layout of an image. If we omit different parts of k-space, the resulting image would better describe the kind and location of data in k-space. Figure 3.4 shows different frequency

¹Considering an image as a $2D$ matrix of size $n \times n$, the center of k-space is $\text{image}(\frac{n}{2}, \frac{n}{2})$.

filters applied to k-space data.

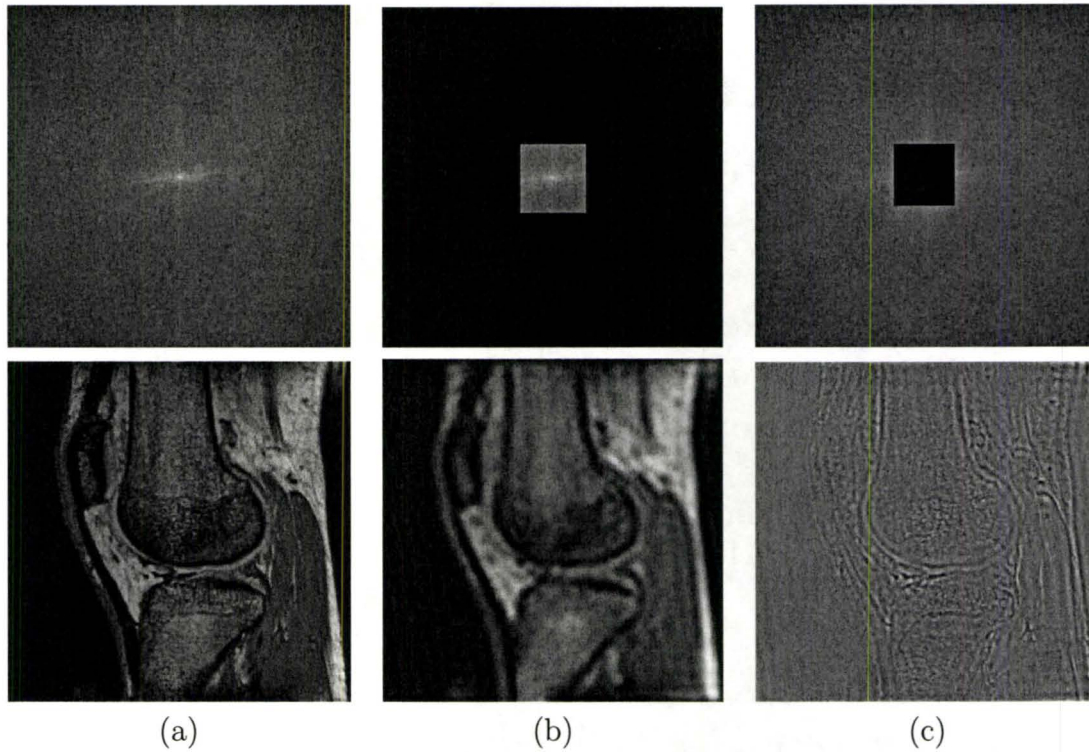


Figure 3.4: Location of certain information in k-space [17] (a) Full k-space with very detailed image (b) Low-pass filter, center of k-space contains low spatial frequencies signals and information of contrast in image (c) High-pass filter, borders of k-space contain high spatial frequencies and information of edges.

The periphery of k-space corresponds to high spatial frequencies in k-space. It is not possible to guess the general layout and edges in an image by examining the visualization of k-space. As an example, Figure 3.5 on page 38 shows four different images with almost the same appearance in k-space yet the result of the inverse Fourier transform turns out to be very different.

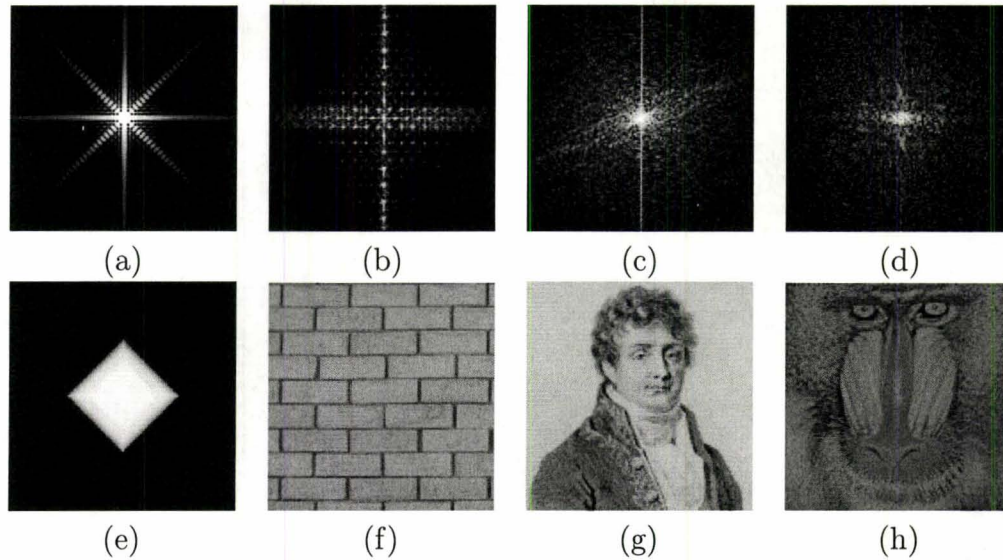


Figure 3.5: Presentation of image in both image-space and k-space (a)-(d)image-space (e)-(f) k-space.

3.2 Full and Partial k-Space

Acquiring complete data (full k-space) is a long and expensive process. Many patients complain about staying still for a long time in a noisy scanner. Even a small movement by the patient during scanning can ruin the whole scanning process, and make unclear and blurry images. It is called motion artifact and results in a strong ghost in the image. There are techniques to reduce scanning time. When the MRI machine tries to scan the entire image, we will get a very detailed and clear image, but it takes a longer time. Partial Fourier reconstruction is a technique that reduces the scanning time by skipping over some data and sampling certain rows of k-space. By reducing the amount of

data to be collected, the scanning time will be reduced dramatically.

MRI machines are capable of scanning certain patterns of data in k-space. Scanning patterns can vary according to the needs and how detailed the image should be. k-Space data is collected row by row, and the MRI machine can easily skip scanning rows and substitute the whole row with zeros. In this case, the k-space appears with a bunch of black lines that correspond to the skipped rows of data.

3.2.1 Half Fourier Projection

Half Fourier or Half Scan is a scanning technique that only samples half the k-space data and then reconstructs the other part of the image from acquired data. Scanners can make use of the conjugate symmetry (figure 3.1 on page 34) of k-space to reduce scan time. It can be done by using the upper or lower part of k-space to reconstruct the other part without any extra scanning. Theoretically the reconstruction of the full k-space can be done only using one quadrant of k-space. The rest of k-space can be created and filled from that, but in practice the conjugate symmetry is not perfect. The noisy environment of the scanner and motion artifacts are obstacles toward using only small data. Figure 3.6 shows the image obtained from half k-space data.

3.2.2 Removing Lines

The most efficient sampling strategy is to interleave rows of k-space with step size k where $1 \leq k \leq \frac{n}{2}$. Figure 3.7 and Table 3.1 better describe partial sampling of k-space. However, undersampling the k-space more than a certain

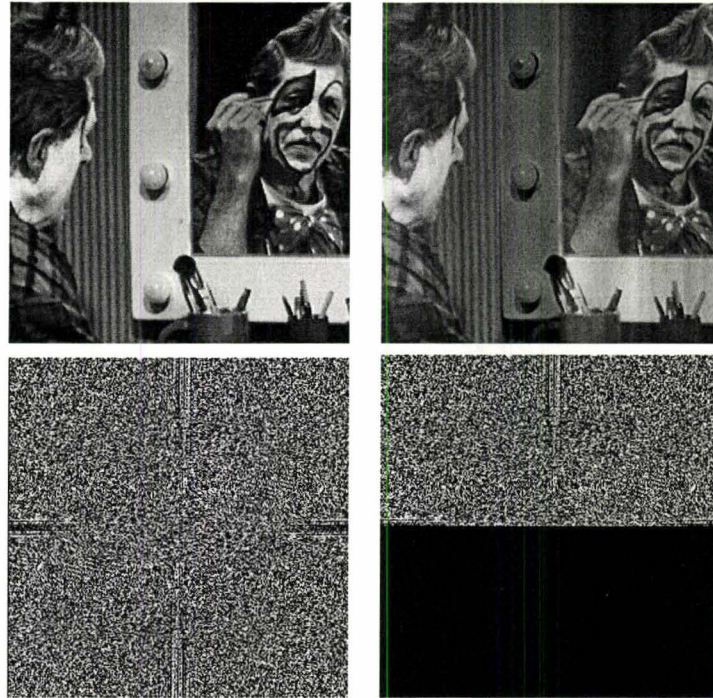


Figure 3.6: Full vs half k-space

amount of data causes unacceptable reconstruction errors. Any distortion or artifact in the image is known as an aliasing error. Figure 3.7.b and 3.7.c show different aliasing problems while undersampling data less than a certain amount. Aliasing may be acceptable if the energy of the alias is lower than the energy of the noise, or if the aliasing is localized away from the anatomy of interest. By sampling sufficient data, the reconstructed image appears without visible artifacts as shown in Figure 3.7.d.

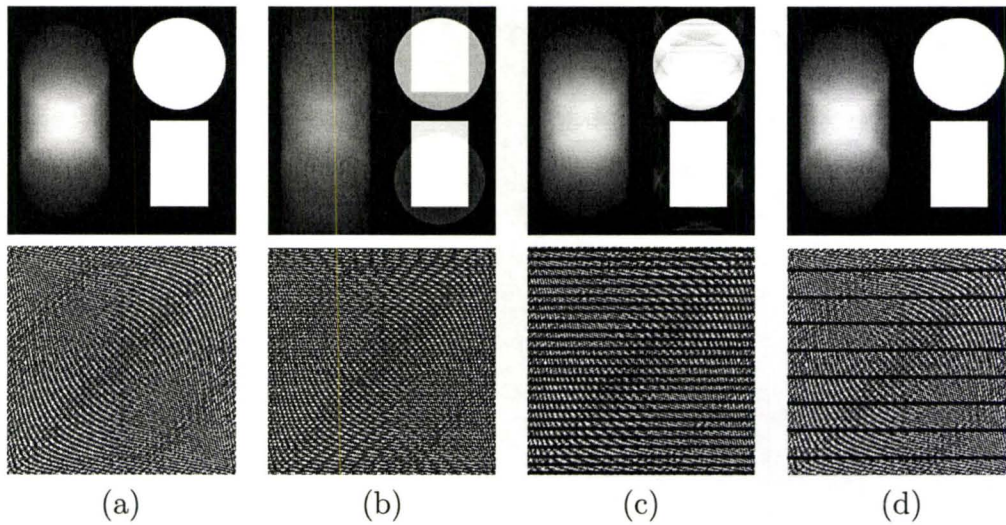


Figure 3.7: Different partial sampling of k-space causes aliasing and artifact in reconstructed image. The corresponding sampling of k-space is presented in Table 3.1.

Experiments	Zero Rows in k-space
Figure 3.7.a	Full k-space
Figure 3.7.b	1/4 Rows: (2, 5, 9,..., n)
Figure 3.7.c	1/10 Rows: (2, 12, 22,..., n)
Figure 3.7.d	1/30 Rows: (2, 32, 62,..., n)

Table 3.1: Different partial sampling of k-space.

Chapter 4

Tissue Quantification

In this chapter, we will present a quantification technique based on the chemical properties of molecules in tissue. This technique is a modification of the Dixon method [8] for fat and water separation in medical imaging. We extended this technique in order to be able to quantify any arbitrary number of tissues. We will show that each MR experiment can be quantified using a linear transformation S from pixel value to tissue concentration. Finally we will explain our tissue quantification technique by an example.

4.1 Quantification Techniques

Tissue quantification refers to the problem of estimating different tissue quantities from a region of interest in an image to build up an anatomical structure. This technique provides very important quantitative information about different tissue types regardless of their physical distribution and can be used in many clinical applications. Tissue quantification can be considered a segmen-

tation strategy, where the acquired image is split into its constituent regions (here tissues). In cases where distinct tissue types are physically well separated and are large relative to image resolution, quantitative tissue volumes have been successfully extracted from qualitative images by different techniques such as active contours (snakes), either manually or automatically. However, these methods of tissue separation are based on selectively suppressing tissue from undesired components, and they are sensitive to main field inhomogeneity. If there is a voxel that contains a portion of multiple tissues together, quantifying each particular tissue is out of reach and is called partial voluming effect. Most quantification methods can only quantify anatomies containing well-separated tissues. Therefore, they are unsuitable for tissues co-located at the image resolution.

Due to various limitations for the existing tissue-quantification methods, a new approach is introduced in this chapter, which modifies and improves the conventional Dixon method [8]. Dixon methods were proposed to separate fat and water in tissues. The result leads to two separate images with improved contrast and a reduction of artifact caused by the interference of fat and water. We observed that we can apply this quantification method in order to quantify any number of tissues.

However, before we get into the technical subtleties, we first introduce the generalized Dixon method, that represents the whole idea of our tissue-quantification technique.

4.2 Tissue Quantification Using the Dixon Method

4.2.1 A Model for Tissue Quantification

For a voxel that consists of m different tissue types with concentrations

$$(\rho_1, \rho_2, \dots, \rho_m) \in \mathbb{R}^m$$

which is imaged n times by varying the pulse sequence, the resulting signals $(I_1, I_2, \dots, I_n) \in \mathbb{C}$, are given by:

$$I_1 = a_{11}\rho_1 + a_{12}\rho_2 + \dots + a_{1m}\rho_m,$$

$$I_2 = a_{21}\rho_1 + a_{22}\rho_2 + \dots + a_{2m}\rho_m,$$

$$\vdots$$

$$I_n = a_{n1}\rho_1 + a_{n2}\rho_2 + \dots + a_{nm}\rho_m,$$

where by definition a complex $I_k = M_x(k) + \sqrt{-1}M_y(k)$ is the projection of the magnetization of the M_{kth} tissue to the $x - y$ plane, which is identified with the complex plane, and $a_{ij} \in \mathbb{C}$ gives the expected signal in image i of a unit quantity of tissue j [42]. Therefore, the coefficient matrix $S^{\mathbb{C}} = ((a_{ij})_{n \times m})$ defines a linear transformation from tissue concentrations to signal measurements. This applies to all voxels equally, and is not dependent on position. For efficient low-level implementation, we do not want to rely on the compiler to handle complex quantities efficiently. If S is considered as a real matrix having twice the number of rows as the complex coefficient matrix $S^{\mathbb{C}} = ((a_{ij})_{n \times m})$ by splitting the real and imaginary parts of a_{ij} into two adjacent rows, and $\text{rank}(S) = m$, then we can invert this linear system to find

the tissue concentration. This is the basic idea of tissue quantification, and we will show how to quantify multiple tissues from multiple images.

4.3 Dixon Method

All imaging methods in MR are based on understanding (and working with) the behavior of solutions to the Bloch equation [3]. The Dixon method uses chemical differences between tissues, which manifest themselves as different external field values, and hence different resonant frequencies. Dixon observed that for fat and water, if one image is acquired while both are in phase and one while they have opposite phases, the resulting images are simple linear combinations of the fat and water components, combined using S :

$$S^c = \begin{pmatrix} 1 & 1 \\ 1 & -1 \end{pmatrix} \quad \text{in the real number format,} \quad S = \begin{pmatrix} 1 & 1 \\ 0 & 0 \\ 1 & -1 \\ 0 & 0 \end{pmatrix} \quad (4.1)$$

In this case an addition and subtraction of acquired images is all that is required to recover the original fat and water concentrations. The difference between the effective excitation and effective measurement time is called echo time. Dixon fixed the phase relation by altering the echo time, but ignored differences caused by relaxation.

Dixon introduced the principle of separating different tissue types by

manipulating the phase relationships, which can be easily extended to more cases than fat and water. The linear transformation S used in the Dixon method are simple by design and therefore usually not written in matrix form. Not doing so obscured the fact that more general linear combinations of tissue densities can be used for tissue quantification.

If there are n experiments and t tissues, S can be presented as a complex matrix of $n \times t$ in (4.2). Each row corresponds to pure tissue concentrations of a certain experiment.

$$S_{n \times t}^C = \begin{pmatrix} a_{11} & a_{12} & \dots & a_{1t} \\ a_{21} & a_{22} & \dots & a_{2t} \\ \vdots & & & \\ a_{n1} & a_{n2} & \dots & a_{nt} \end{pmatrix} \quad (4.2)$$

4.3.1 An Example

In order to better understand how the Dixon method quantifies tissues even when a voxel contains mixture of multiple tissue values (partial volume effect), we use a simple example. Having the experiments, we are trying to separate each tissue from each voxel using S . This is the problem we want to solve. The forward problem would be to build MR images having pure tissue values and S transformation. Each pixel in MR image is built up of the linear combination of different tissues:

$$I_n = a_{n1}\rho_1 + a_{n2}\rho_2 + \dots + a_{nm}\rho_m, \quad (4.3)$$

where ρ_i is pure tissue i and a_{nm} is element of $S^{\mathbb{C}}$. The transformation used to generate experiments, (S) , is defined as a matrix containing complex numbers. Elements of S are the density of pure tissues in their corresponding experiment.

Figure 4.1 is a 2D view of three geometric phantoms. These grayscale pictures represent MR images and each one contains a distinct tissue. In chapter 6 we will present a 3D view of phantom in a layer of body.

This example is to better understand the use of the generalized Dixon method and the transformation S . By having the portion of pure tissue in each voxel, we can set the density of tissues in all voxels. By adding all densities of all tissues together in a voxel, we will be able to build the MR experiments.

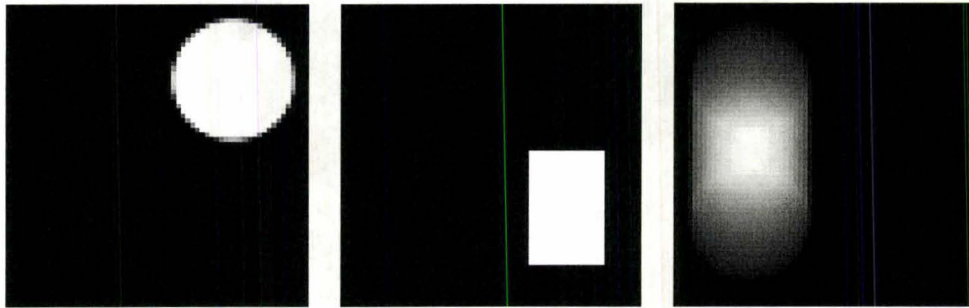


Figure 4.1: Three simulated tissue fractions (ρ_1, ρ_2, ρ_3) shown in separate images.

4.4 Specifying the Transformation S

Each experiment has a specific transformation. If there are n experiments and t distinct tissues, S will be an $n \times t$ matrix and each row corresponds to one of the experiments as shown in Figure 4.2. Each entry of S represents the

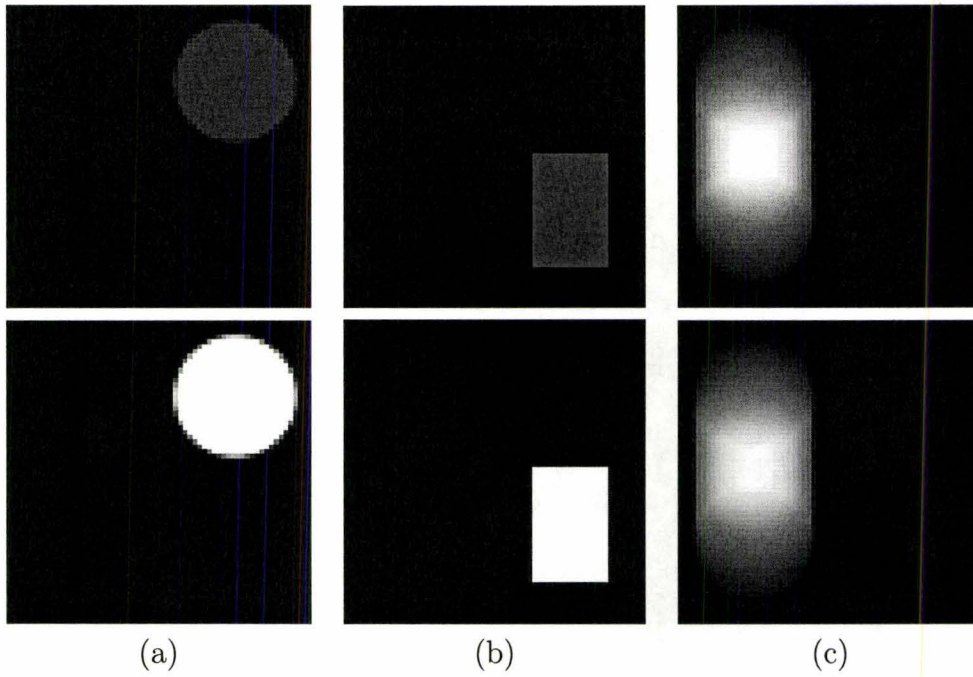


Figure 4.2: Having the portion of each tissue in each voxel, we can find the density of each voxel in different experiment. Real and imaginary parts for one experiment for each tissue after applying the S transformation.

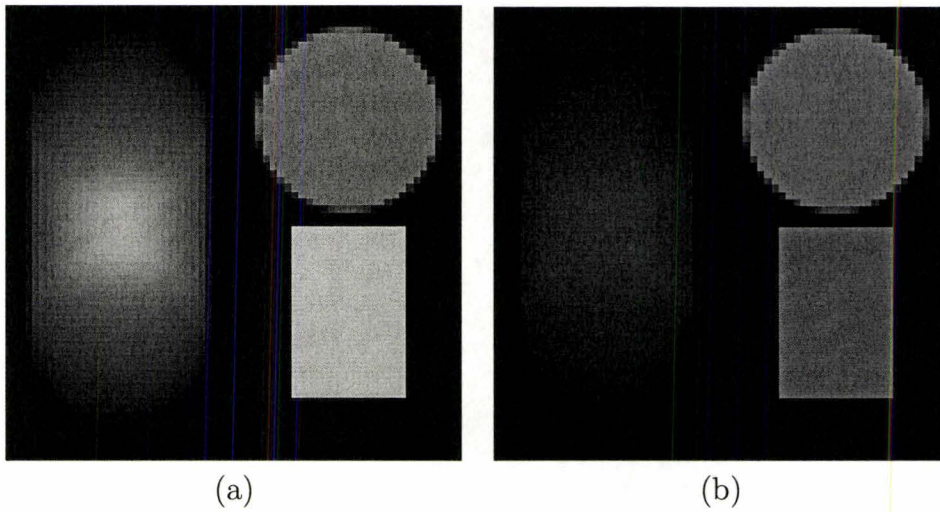


Figure 4.3: Linear combination of tissue using S . (a) Real part (b) Imaginary part

concentration of a pure tissue in a certain experiment. As an example, a_{ij} is the concentration of pure tissue j in experiment i . A simple way of finding a_{ij} is to manually specify a pixel in the acquired image i in a region that only contains pure tissue j and figure out the pure tissue concentration. This can be done either manually by a medical technician or radiologist, or by means of a machine learning algorithm, which we consider as a future work of this thesis. In chapter 5, S transformation is used in the modeling of the segmentation problem. More details about the structure and elements of S will be discussed later.

Chapter 5

Inverse Problems

In this chapter, we present a new model to solve the tissue-quantification problem. Medical image processing is a well-suited platform to propose inverse problems. Having the medical images, we are looking for the causes, such as cancer detection. To better understand the concept of inverse problems, first we explain how to build up images from segmented tissue, using forward problems. Then we discuss how to model our problem as an inverse problem. Regularization can be used to make an ill-posed problem well-posed [12]. Here we used regularization both for noise reduction and to remove the singularity caused by ill-conditioning [40] and [34].

5.1 Forward Problem

The forward problem tries to find the effect and the result of interaction between different elements of a system in a straightforward way. As an example, consider three rivers with a certain amount of water flowing that merge in a

lake. If we know the exact amount of water in each river, we can easily estimate the total amount of water accumulated in the lake. Here the elements of the system are amount of water and number of rivers, and the interaction between them results in a certain amount of water in the lake.

Let t be the number of different tissues in the target anatomy. We are given n images, $C_j : Z^2 \rightarrow R$; each containing the per-pixel concentration of a single tissue, where the pixels are indexed by pairs of integers in Z^2 . The forward problem is to find the expected MR images, I_i . In other words, knowing the number of experiments, we try to mix all these t pure tissue images in order to make MR experiments. We can easily solve this problem by having the S matrix (explained in chapter 4) that specifies the contribution of each tissue in different experiments:

$$I_i = S C_i \tag{5.1}$$

where this product is to be understood as a pointwise product operating in parallel on each pixel.

5.2 Inverse Problem

Any time we want to know model variables based on experimental measurements with a known mathematical model connecting variable values to expected experimental outcomes, we have an inverse problem. As a diagram:

$$\text{Data} \rightarrow \text{Modeled Parameter} \tag{5.2}$$

5.2.1 Linear Inverse Problem

In this class of problem, the relationship between data and modeled variables is linear, *e.g.*

$$Ax = b \tag{5.3}$$

where A is a linear operator, and b and x represent data and model parameters and the job is to find x . Our quantification problem can be described this way.

In other words, having the MR experiments, we are trying to find the tissue fractions that would result in the observed images. We can define an optimization problem in which the objective function measures the likelihood of observing image pixel values given underlying tissue concentrations. If the measurement error is independent and normally distributed, then this is the L_2 distance between the measured MR experimental images and the images predicted by the forward problem. When we only collect partial k-space data, we have to include the effect of the Fourier transform. The job is to solve a least-squares problem. In other words, we minimize the distance between the measured MR experimental images and the images predicted by the forward problem.

5.2.2 Linear Least Squares

The linear least squares problem is to find a solution x to

$$\|Ax - b\|^2 = \min$$

for given $A \in R^{m,n}$ and $b \in R^m$. This problem might be view as a generalization of the linear equation $Ax = b$, since for invertible A the solutions coincides. However, if A is not invertible, the linear equation does not have a solution, while the least problem always has a solution. Moreover, if the column rank of the matrix A is full, the solution is unique and given by

$$x = \frac{(A' * A)}{(A' * b)}$$

A linear least squares approach is a natural choice for a linear data fitting problems since it enables the handling of inconsistent data. However, for some inverse problems the above solution may still depend too much of the data and hence additional regularization becomes essential. This topic is addressed in Section 5.4 in more detail.

In the following section we will describe each component of our least-squares problem in detail.

5.3 Modeling the Quantification Problem

Considering the general form of an inverse problem in (5.3), we describe the quantification problem, where b is the experimental data collected from MRI scanners which is both incomplete and noisy with white Gaussian noise in k-space. In order to consider the effect of incomplete data (partial k-space) b needs to be in Fourier space. Therefore, we need to use a Fourier transformation in our modeling strategy. A is a transformation from pure tissue to pixel values. We used the S transformation in the Dixon method described in

chapter 4. In order to make both sides of equation (5.3) in the same space, A also needs to include the effect of Fourier transformation. Finally, the modeled parameters, x , are the fractions of pure tissues in each voxel. Having A and b , the task is to find x in a way that fit in (??).

In case of least-squares problem, $\|Ax - b\|_2^2$, A and b are described as follow:

$$A = P \cdot FT \cdot S_p \quad (5.4)$$

$$b = P \cdot FT \cdot I_i, \quad (5.5)$$

where the projection onto partial data P , the Fourier transform FT , and the block form of S are explained in the following section.

5.3.1 Projection P

The phantoms used here are completely sampled in k-space. We can simulate the partial k-space data by projecting the full k-space data onto a subspace. It is possible to sample different patterns of data in a way similar to that of a MRI scanner.

$$\text{projection} \times \text{full k-space} = \text{partial k-space}$$

The projection can be done by zeroing rows of $FT \times S$ that correspond to k-space rows not collected. This approach enables us to choose a variety of

projection matrices for each specific experiment. If e is the number of different MR experiments, P is a block-diagonal matrix with e blocks of projection. Each block initially is an identity matrix where zeros are placed on the diagonal in order to indicate unsampled rows in k-space (simulate partial k-space). Each block presents the sampling map for a certain experiment. Figure 5.1 shows the structure of block-diagonal P matrix for e experiments.

$$P = \begin{pmatrix} \begin{pmatrix} \text{Experiment 1} \end{pmatrix} & & & \\ & \begin{pmatrix} \text{Experiment 2} \end{pmatrix} & & \\ & & \ddots & \\ & & & \begin{pmatrix} \text{Experiment e} \end{pmatrix} \end{pmatrix}$$

Figure 5.1: Structure of block-diagonal matrix P for e experiments.

In order to show different phases and frequencies of MR signals, all the acquired data are complex. We separate the real and imaginary part of all complex numbers in order to use real-valued linear algebraic operations. Real arithmetic enables us to also implement the solver efficiently in other programming languages such as C. However, separating real and imaginary parts of data doubles the number of rows in P . C is a complex number and

R represents the same number with separated real and imaginary parts.

$$C = \alpha i + \beta, \quad R = \begin{pmatrix} \alpha \\ \beta \end{pmatrix} \quad (5.6)$$

In this case, P contains pairs, $\begin{pmatrix} 1 & \\ & 1 \end{pmatrix}$ or $\begin{pmatrix} 0 & \\ & 0 \end{pmatrix}$, depending on whether a row of k -space is selected or not. Figure 5.2 shows how to separate the elements of P .

$$\begin{pmatrix} 1 & & & & \\ & 0 & & & \\ & & 1 & & \\ & & & 0 & \\ & & & & 1 \end{pmatrix}_{5 \times 5} \rightarrow \begin{pmatrix} 1 & & & & & & & & & \\ & 1 & & & & & & & & \\ & & 0 & & & & & & & \\ & & & 0 & & & & & & \\ & & & & 1 & & & & & \\ & & & & & 1 & & & & \\ & & & & & & 0 & & & \\ & & & & & & & 0 & & \\ & & & & & & & & 1 & \\ & & & & & & & & & 1 \end{pmatrix}_{10 \times 5}$$

(a)
(b)

Figure 5.2: A sample 5×5 block of P . (a) Sampling complex data (b) Sampling data with separated real and imaginary part.

However, removing rows from k -space may cause A to be singular, i.e., not invertible. We can reduce the size of the matrix by deleting the rows in P blocks that contain zeros, thereby saving many extra computations (without requiring the use of sparse linear algebra). Figure 5.3 shows the compressed matrix for each block of P .

$$\begin{array}{ccc}
 \begin{pmatrix} 1 & 0 & 0 & 0 & 0 & 0 \\ 0 & 1 & 0 & 0 & 0 & 0 \\ 0 & 0 & 0 & 0 & 0 & 0 \\ 0 & 0 & 0 & 0 & 0 & 0 \\ 0 & 0 & 1 & 0 & 0 & 0 \\ 0 & 0 & 0 & 1 & 0 & 0 \\ 0 & 0 & 0 & 0 & 0 & 0 \\ 0 & 0 & 0 & 0 & 0 & 0 \\ 0 & 0 & 0 & 0 & 1 & 0 \\ 0 & 0 & 0 & 0 & 0 & 1 \end{pmatrix} & \rightarrow & \begin{pmatrix} 1 & 0 & 0 & 0 & 0 & 0 \\ 0 & 1 & 0 & 0 & 0 & 0 \\ 0 & 0 & 1 & 0 & 0 & 0 \\ 0 & 0 & 0 & 1 & 0 & 0 \\ 0 & 0 & 0 & 0 & 1 & 0 \\ 0 & 0 & 0 & 0 & 0 & 1 \end{pmatrix} \\
 (a) & & (b)
 \end{array}$$

Figure 5.3: Removing the singularity of matrix P by deleting rows with zeroes on the diagonal.

5.3.2 Fourier Transformation FT

If e is the number of experiments, FT is a block-diagonal constant matrix of 1D Fourier transformations with e blocks. Since we either fully sample or do not sample rows, the error associated with raw data and data transformed in the row direction are both independent, identically distributed Gaussian noise. We can reduce the problem size significantly if we consider one or a small number of columns at a time, but using row-transformed data in the model rather than raw data. In all our computations, we separate the real and imaginary parts of all elements. To perform only real computations, the real and imaginary parts are separated, and the complex elements of the FT

are replaced by 2×2 blocks:

$$ft = \begin{pmatrix} \cos(\alpha) & -\sin(\alpha) \\ \sin(\alpha) & \cos(\alpha) \end{pmatrix} \quad (5.7)$$

$$\alpha = -2\pi \times (i - 1) \times (j - 1)/n; \quad i, j = 1 \dots n$$

Since we sample different rows in k-space for each experiment, the product $(P \cdot FT)$ with zero rows removed varies from image to image. The product $(P \cdot FT)$ also is a block-diagonal matrix with e blocks, and each block represents a specific Fourier transform for each partially sampled experiment. Figure 5.4 shows the product $(P \cdot FT)$

$$P \cdot FT = \begin{pmatrix} \begin{pmatrix} \text{FT} \\ \text{Experiment 1} \end{pmatrix} & & & \\ & \begin{pmatrix} \text{FT} \\ \text{Experiment 2} \end{pmatrix} & & \\ & & \ddots & \\ & & & \begin{pmatrix} \text{FT} \\ \text{Experiment e} \end{pmatrix} \end{pmatrix}$$

Figure 5.4: The product $(P \cdot FT)$ is also a block-diagonal matrix.

5.3.3 Pixelwise S_p Transformation

S is a pixelwise matrix¹ and we will use the same letter for the transformation from tissue density to pixel values for particular experiments, and for the block-matrix generalization, which would be block diagonal with identical blocks in

¹A pixelwise matrix can be transformed by reordering coordinates into a block-diagonal matrix with identical blocks, where each block acts on a single pixel.

a basis where the elements corresponding to a single pixel value are gathered together. We define t as the number of different tissues and e as the number of experiments. Each element of S ($a_{ij} \in \mathbb{C}$) is a complex number that represents the signal produced by pure tissue j in experiment i . Figure 5.5 shows the format of matrix S .

$$S = \begin{matrix} & \text{T1} & \text{T2} & \dots & \text{Tt} \\ \text{Exp 1} & a_{11} & a_{12} & \dots & a_{1t} \\ \text{Exp 2} & a_{21} & a_{22} & \dots & a_{2t} \\ \vdots & \vdots & & & \vdots \\ \text{Exp e} & a_{e1} & a_{e2} & \dots & a_{et} \end{matrix}$$

Figure 5.5: Matrix S indicates the signal produced by pure tissue for different experiments where $\text{Exp}i$ represents different experiments and Ti represents different tissues.

We define a new matrix S_p that rearranges the elements of S in order to fit in our least-squares problem. Remember that each element of S is a complex number, and we have to separate real and imaginary part as shown in (5.6).

5.3.4 Experimental Data b

We are trying to find modeled parameter (x) in a way to minimize the distance between approximated data ($P \cdot FT \cdot S_p \cdot x$) and experimental data (b). Therefore, b must be in the same space as the approximated data. It means b has to be in Fourier space and uses the same projection P . In other words, b is the row Fourier transform of the collected rows in k-space, which for the numerical simulation are generated by taking column transforms of ideal images

$$S_p = \begin{pmatrix} \begin{pmatrix} R_{11} & & \\ & R_{11} & \\ & & \ddots \\ & & & R_{11} \end{pmatrix} & \begin{pmatrix} R_{12} & & \\ & R_{12} & \\ & & \ddots \\ & & & R_{12} \end{pmatrix} & \dots & \begin{pmatrix} R_{1t} & & \\ & R_{1t} & \\ & & \ddots \\ & & & R_{1t} \end{pmatrix} \\ \begin{pmatrix} R_{21} & & \\ & R_{21} & \\ & & \ddots \\ & & & R_{21} \end{pmatrix} & \begin{pmatrix} R_{22} & & \\ & R_{22} & \\ & & \ddots \\ & & & R_{22} \end{pmatrix} & \dots & \begin{pmatrix} R_{2t} & & \\ & R_{2t} & \\ & & \ddots \\ & & & R_{2t} \end{pmatrix} \\ \vdots & \vdots & \dots & \vdots \\ \begin{pmatrix} R_{e1} & & \\ & R_{e1} & \\ & & \ddots \\ & & & R_{e1} \end{pmatrix} & \begin{pmatrix} R_{e2} & & \\ & R_{e2} & \\ & & \ddots \\ & & & R_{e2} \end{pmatrix} & \dots & \begin{pmatrix} R_{et} & & \\ & R_{et} & \\ & & \ddots \\ & & & R_{et} \end{pmatrix} \end{pmatrix}$$

Figure 5.6: Matrix S_p , having t different tissues and e MR experiments. $R_{l,m}$ is $a_{l,m}$ in the 2×1 block format shown in (5.6).

with noise added, and projecting out the unsampled rows. Using the same P and FT , b is defined as follows:

$$b = P \cdot FT \cdot I_i \tag{5.8}$$

where I_i is the simulated MR data.

5.3.5 Solver

We implemented our algorithm using Matlab. We used the linear least-squares function (`lsqin`) as a solver for our optimization problem. `lsqin` is used to

solve constrained linear least-squares problems. The function call and each argument is described here:

$$x = \text{lsqin}(A, b, C, d, Aeq, beq, lb, ub) \quad (5.9)$$

where

$$\min_x \|A \cdot x - b\|_2^2, \text{ such that, } \begin{cases} C \cdot x \leq d, \\ Aeq \cdot x = beq, \\ lb \leq x \leq ub. \end{cases} \quad (5.10)$$

The objective is to minimize the distance between segmented tissues and multiple MR experiments. Solving the problem for multiple images in one step results in a very large and sparse system. For example, if the image size is $n \times n$ and we have e experiments with t tissues, the size of A and b in equation (5.10) will be approximately:

$$A \approx 2 \cdot n^2 \cdot e \times n^2 \cdot t \quad (5.11)$$

$$b \approx 2 \cdot n^2 \cdot e \times 1 \quad (5.12)$$

which requires more than available memory, even for moderate image sizes (128×128). Table 5.1 shows the size of the least-squares problem for different image sizes.

However, we can split the problem into smaller parts and solve it for k columns of the image at a time and cover the whole image through iteration. The simplest case is when $k = 1$. Depending on the regularization method being used, k can be chosen in the interval $1 \leq k \leq \lfloor N/2 \rfloor$. If we call s the

Image Size	Size of A	Size of b
32×32	8192×3072	4096×1
64×64	32768×12288	16384×1
128×128	131072×49152	65536×1
256×256	524288×196608	262144×1
512×512	2097152×786432	1048576×1
1024×1024	8388608×3145728	4194304×1

Table 5.1: Solving the problem in a single step, rather than several columns at a time, results in very large matrix sizes in $\|Ax - b\|_2^2$.

step size, each iteration segment s column of the image ($s < k$). However, at the end of the iterations, there might be cases where the set of columns left are less than k . In other words, if the iterations pass $N - k$, there are less columns to be chosen in sets of size k . This problem can be recovered by appending extra zero columns at the end of the image. Although, there is a trade-off between the number of appended zero columns and the clarity of the segmented images at the image borders. The bigger the k , the better and more accurate the segmentation, but there is less image clarity at the borders of the image. Depending on the choice of regularization method, our algorithm is capable of solving the problem for different numbers of columns (k 's). We obtained good results by picking $k = 4, 6, 8$. Figure 5.7 shows the pseudo-code for the segmentation problem iterating through column groups.

By this approach, we reduce the size of A and b to acceptable sizes for $lsqlin()$. It also allows parallel computation using a number of processors which can scale linearly with the image width. We consider solving the problem

```
[tissues] = Quantification(images,k,s)
A = P(n,k) * FT(n,k) * Sp(n,k);
for i = 1 : imageSize with Step Size s;
    tissues = lsqlin(A, Column i to i+k of Image);
end;
```

Figure 5.7: Pseudo-code for segmentation k columns at a time, where $P(n,k)$, etc., set up the block matrices for images of size $n \times k$.

in parallel as future work.

5.3.6 Constraints

Since tissue density is expected to be non-negative, and the sum of all tissue densities in a voxel is bounded by voxel size, it would make sense to introduce linear constraints into the least-squares problem, thereby reducing the expected noise. In particular, we have made some experiments with non-negativity constraints on tissue concentrations, but the best form for doing this is still an open question.

5.4 Regularization

We start by making some comments on ill-posed problems. A problem is called well-posed in the sense of Hadamard [12], If $A : X \rightarrow Y$ and $Ax = y$, a mathematical problem is well posed when:

1. For each datum y in a given class of function Y there exists a solution x in a prescribed class X such that $Ax = y$ (Existence);

2. The solution x is unique in X . $Ax_1 = Ax_2 \rightarrow x_1 = x_2$ (Uniqueness);
3. The dependence of x upon y is continuous, i.e., when the error on the data y tends to zero, the induced error on the solution x tends also to zero which means A^{-1} is continuous (Continuity).

If a problem does not satisfy one of these three conditions, it is called an ill-posed problem. Inverse problems are not usually well posed, and in order to be solvable, a variety of regularization techniques can be applied to solve the problem [2]. There are many regularization techniques available and are categorized in to three classes:

- optimization-based
- filtering-based
- iteration-based

The linear least squares problem (5.2.2) always has a solution. However, it is not necessarily well-posed, i.e. the solution may not be unique and it can be very sensitive to the data. In the presents of noise, unexpected results can thus be observed. Remedies are to add a regularization which makes the solution unique or to add a penalty which out rules unwanted solutions. To begin with, we pick the simplest Tichonov regularization. The regularized problem thus reads

$$\|Ax - b\|^2 + \alpha\|x\|^2,$$

where $\alpha > 0$ is the regularization parameter.

5.5 Tikhonov Regularization

One of the easily designed regularization methods for linear problems is Tikhonov regularization [35]. It is also known as ridge regression.

Assume X, Y are Hilbert spaces² where $x \in X$ and $b \in Y$. A linear system is defined by the following equation:

$$Ax = b + \eta \tag{5.13}$$

where η is noise in the experiment. From the linear point of view, A is an $m \times n$ matrix, x is a column vector of length n , and b is a column vector of length m . If $m > n$, the problem is to find an approximate solution of an overdetermined system by minimizing

$$T(x) = \|Ax - b\|_2^2 + \alpha P(x), \tag{5.14}$$

for some penalty function P . When the penalty is quadratic, we can write the problem as

$$x_\alpha \in \underset{x \in X}{\operatorname{argmin}} \|Ax - b\|_2^2 + \alpha \|Rx\|_2^2 \tag{5.15}$$

x_α is an approximate solution to the fit-to-data term $\|Ax - b\|_2^2$, depending on the penalty weight, α .

Since our problem is linear and finite dimensional, we can consider linear penalty functions as a matrix R with α weighting. In this case, all penalties

²Hilbert space generalizes the notion of Euclidean space in a way that extends methods of vector algebra from the two-dimensional plane and three-dimensional space to infinite-dimensional spaces.

and fit-to-data terms can be combined in a single least-squares minimization. Equation 5.16 shows the merged least-squares problem.

$$\begin{aligned} & \|Ax - b\|_2^2 + \alpha \|Rx\|_2^2 \rightarrow \\ & \left\| \begin{pmatrix} A \\ \alpha R \end{pmatrix} x - \begin{pmatrix} b \\ 0 \end{pmatrix} \right\|_2^2. \end{aligned} \quad (5.16)$$

In the case that R is the identity and α is strictly positive, we can write

$$x_\alpha = (A^*A + \alpha I)^{-1} A^*b \quad (5.17)$$

5.5.1 Choice of Regularization Operator R

The penalty term is sometimes called a discrete smoothing norm. It indicates that high frequencies in the solution are penalized and converge to zero, but low frequencies remain unregularized. It behaves as a low-pass filter.

In Tikhonov regularization, the operator R is usually I , an identity matrix of $n \times n$ (considering $A_{m \times n}$ in 5.16). Different weightings are applied to R through α , the regularization parameter. In our segmentation problem we used the L_2 norm of the differences of neighbours in both column and row directions. We can subtract each pixel from the neighbors in both row and column directions. We can substitute a pixel value by average of neighbor pixels. We discuss each case in detail.

$$Col = \begin{pmatrix} 1 & -1 & & & & \\ & 1 & -1 & & & \\ & & \ddots & \ddots & & \\ & & & 1 & -1 & \\ & & & & 1 & \\ & & & & & \ddots \\ & & & & & & 1 & -1 \\ & & & & & & & 1 \end{pmatrix}_{n \times n}$$

Figure 5.8: *Col* matrix used to regularize image in column direction

Regularization in Column Direction

In this case, the term R , named *Col*, should be designed in a way that by multiplying it to pure tissue vector x , subtract current pixel value from its lower neighbor pixel. For this means, we use an identity matrix of size $n \times n$ with -1 on upper sub-diagonal. Figure 5.8 shows the structure of the matrix for regularization in the column direction.

Regularization in Row Direction

Regularization can also be done in the row direction. In this case we use the right neighbor of each pixel to regularize the current pixel value. The matrix needed here is the vertical concatenation of two matrices. The first one is an identity matrix and the second one is an identity matrix with -1 coefficient. We name this block *Row* with the size $n \times 2n$. By multiplying this block to the vector of pure tissue, each pixel value is substituted by its value being subtracted from its neighboring pixel value. In Figure 5.9, the structure of the row regularization matrix is illustrated.

We described the simple block of *Row* and *Col*. We have to combine

$$Row = \left(\begin{array}{cccc|cccc} 1 & & & & -1 & & & \\ & 1 & & & & -1 & & \\ & & \ddots & & & & \ddots & \\ & & & 1 & & & & -1 \\ & & & & 1 & & & -1 \end{array} \right)_{n \times 2n}$$

Figure 5.9: *Col* matrix used to regularize image in column direction

these 2 blocks together as follows:

$$R = \begin{pmatrix} Col \\ Row \end{pmatrix}_{2n \times 2n} \quad (5.18)$$

Remember that in the solution we proposed earlier, we processed multiple columns of an image at a time. In the least-squares solver, if we process k columns at each iteration, we need k blocks of *Col* and $k - 1$ blocks of *Row*.

As an example, if $k = 4$ the structure of $\begin{pmatrix} A \\ R \end{pmatrix}_{2m \times 2n}$ in (5.16) is as figure 5.10.

5.5.2 Regularization Parameter

The regularization parameter α must be chosen in order to balance the need to fit the experimental data and the a priori information represented by the penalty term. There is no specific range for variation of α . There are regularization-parameter selection techniques that have been proposed in the literature in order to find a good regularization term α . Techniques such as the *L-curve*

$$\left(\begin{array}{cccc} (A) & & & \\ & (A) & & \\ & & (A) & \\ (Col) & & & (A) \\ & (Col) & & \\ & & (Col) & \\ & (Row) & & \\ & & (Row) & \\ & & & (Row) \end{array} \right)_{n \times 2n}$$

Figure 5.10: Regularizing operator R consists of both row and column regularization.

method, cross validation, discrepancy principle and unbiased predictive risk estimator. In the following, we explain some of these techniques and L-curve parameter selection in detail for our regularization problem.

Discrepancy Principle

If δ is the expected value of $\|e\|_2$, then the regularization parameter should be chosen so that the norm of the residual corresponding to the regularized solution $\|x_{reg}\|$ is $\tau\delta$ [19], [26]; that is,

$$\|Ax_{reg} - b\|_2 = \tau\delta \quad (5.19)$$

where $\tau > 1$ is some predetermined real number. It is obvious that $\delta \rightarrow 0$, $x_{reg} \rightarrow x_{true}$. For example, if the signal-to-noise ratio is known, this method

could be used.

L-curve

The L-curve for a Tikhonov-regularized solution of an ill-posed problem is a parametric plot of the norm of the regularized solution with stabilizer parameter $\|Rx_\alpha\|_2$ versus the corresponding residual norm for each set of parameter values $\|Ax_\alpha - b\|_2$, and was introduced by Lawson [21] and popularized by Hansen [13]. Figure 6.16 shows a sample plot of an L-curve in the plane of $\|Ax_\alpha - b\|_2$, $\|Rx_\alpha\|_2$. The L-curve thus gives insight into the properties of the underlying regularization method, and it is used to determine an optimal regularization parameter α for the given data.

5.5.3 Determination of the Regularization Parameter via the L-curve Approach

Considering the first derivative with respect to α of $\|Ax_\alpha - b\|_2^2$ and $\|Rx_\alpha\|_2^2$, $\|Rx_\alpha\|_2^2$ monotonically decreases with respect to α while $\|Ax_\alpha - b\|_2^2$ monotonically increases with respect to α . This defines a correspondence between $\|Ax_\alpha - b\|_2^2$ and $\|Rx_\alpha\|_2^2$ which when plotted parametrically defines a curve, known as the L-curve, because of the shape it commonly takes.

Choosing a good α can be done by considering a trade-off between accuracy and the smoothness of the solution. Depending on various regions of interest, different α 's can be chosen for different purposes. As an example, the regularization parameter for smoothing background in an image needs to be larger than α for regularizing edges.

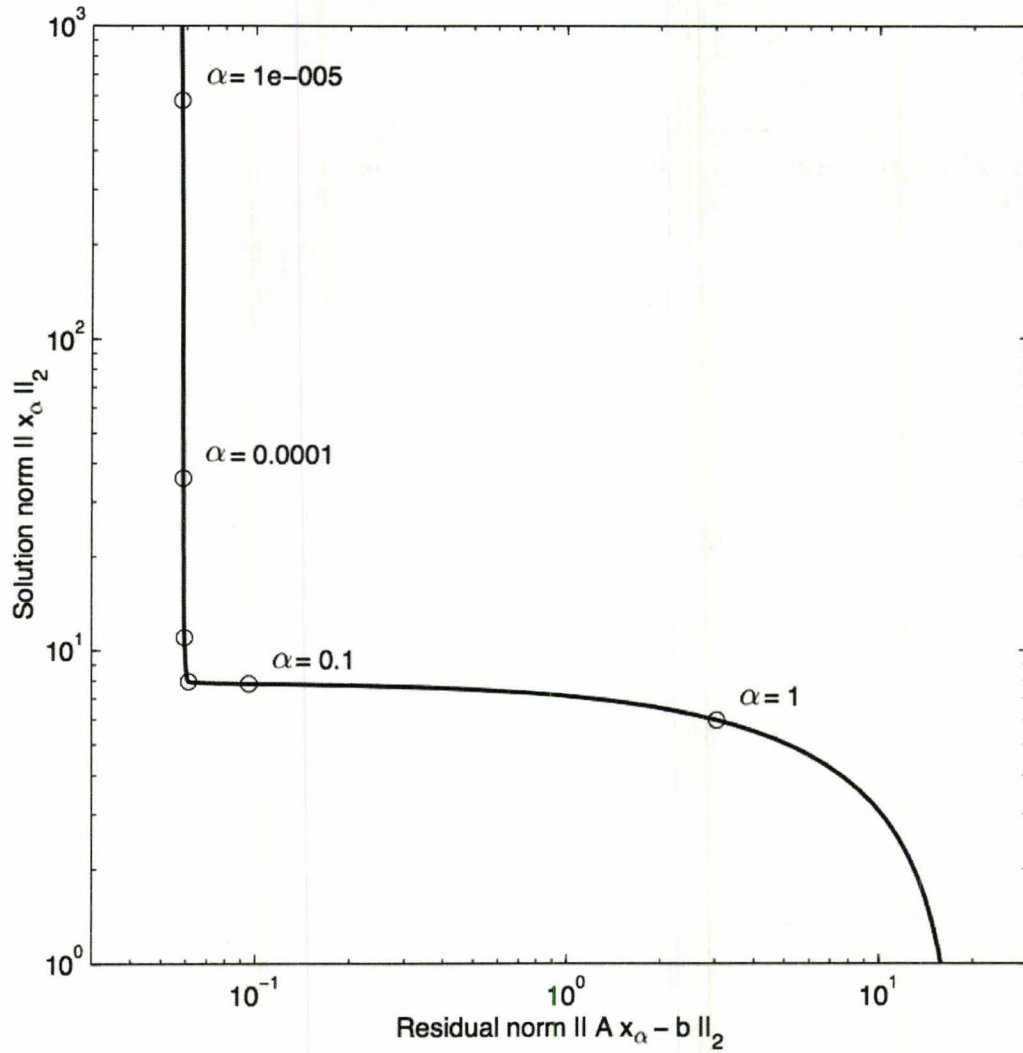


Figure 5.11: The L-curve for standard form Tikhonov regularization [14]. The points marked by circles correspond to different regularization parameters, α .

We define two parameters r_α and s_α below, in order to better illustrate

the trade-offs between accuracy and smoothness of a regularized solution.

$$r_\alpha = \|Ax_\alpha - b\|_2^2 \quad (5.20)$$

$$s_\alpha = \|Rx_\alpha\|_2^2 \quad (5.21)$$

where the residual r_α determines the accuracy of the solution while s_α determines the smoothness of the solution. Clearly, the smaller the r_α , the better and more accurate the solution for (5.20); and also the smaller s_α , the smoother the solution.

The behavior of the L-curve with respect to α was explained by Lung and Lu in [23]. If A and R can be simultaneously decomposed, *i.e.*, with the same eigen- or singular-vectors, then the terms r_α and s_α , and their derivatives with respect to α , can be expanded in series depending on the singular values, from which the high and low slopes in the L-curve follow by taking limits.

Considering a sample plot of the L-curve in Figure 6.16, the left portion of the L-curve behaves as a vertical line and hence its curvature is small. It is obvious that any point on this portion of the L-curve corresponds to a x_α with good solution accuracy (*i.e.* small r_α) but poor smoothness. For large values of α , s_α and its derivatives are small while r_α is independent of α . The right portion of the L-curve corresponds to bigger α 's and large r_α . The curvature in that part of the curve is small. It means this part of the curve has x_α with smooth points yet poor solution accuracy.

Considering the trade-off between smoothness and accuracy of x_α , the best α is located at the very corner of the curve.

We can summarize the steps toward finding a good α as follows:

1. Calculate various number of points ($\|Ax_\alpha - b\|_2^2$, $\|Rx_\alpha\|_2^2$) for varying α over a wide range of data.
2. Plot the points, and interpolate parametrically if necessary.
3. Choose a value of α giving a point in the expected range for the fit-to-data and penalty terms and relatively more curvature by inspection.

Considering the behavior of the L-curve and how it alters the solution of the least-squares problem, we can consider it as a filter which filters out singular components that are small (relatively) while retaining components that are large. In this sense, it is called a Tikhonov filter. In the next chapter we will show how Tikhonov filtering affects the results. It helps us overcome the inaccurate segmentation caused by noisy and partial MRI data acquisition, yet makes the results look smoother and clearer.

Chapter 6

Numerical Results

In this chapter, we present the results of a proposed algorithm and show how regularization improves the results.

6.1 Geometrical Phantoms

We simulated three tissue numerical phantoms with simple geometrical shapes, including partial volume effects¹. It includes a cylinder obliquely intersecting the image plane, a cube, and a sphere representing separate tissues. Figures 6.1 and 6.2 show each tissue and their combination.

¹There might be situations where each voxel in the images represents more than one tissue type. This phenomenon is referred to as the partial-volume effect.

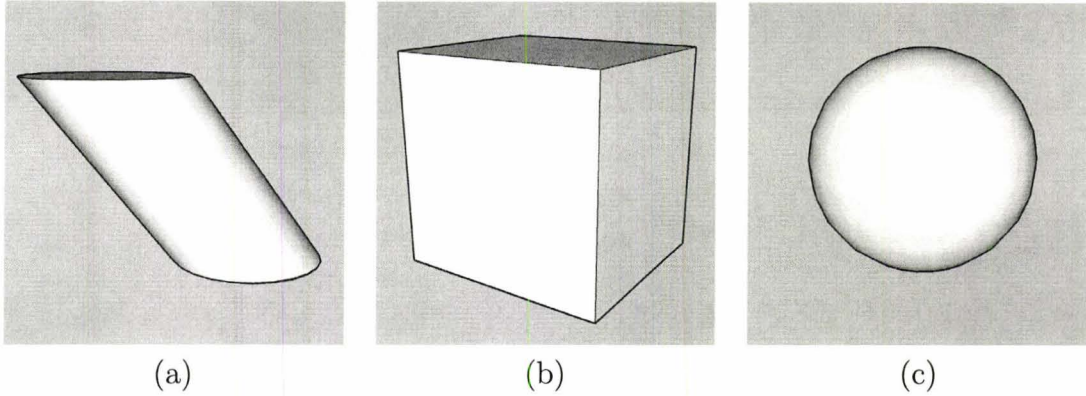


Figure 6.1: Geometrical phantoms representing different tissues in a target anatomy. An oblique cylinder, a box, and a sphere in one layer.

Recall from the first chapter that an MR image shows different tissues within a layer of the body with a certain thickness. We simulated each layer by a 3D volume that is shown in Figure 6.3. In order to be able to process the layer, we have to flatten the 3D layer to obtain a 2D MR image of size $n \times n$. We can approximate the tissue concentration of each voxel² by splitting it into subvoxels shown in Figure 6.3 and find the sum of the subvoxels that belong to a certain tissue. Each voxel is of size $l \times w \times a$ where l is the length, w is the width and a is the height. If the the image size is $n \times n$, the tissue concentration of pixel (i, j) of tissue t can be calculated by dividing the number of subvoxels containing tissue t at their centers by the total number of subvoxels.

Each voxel has a value between 0 and 1 ($0 \leq voxel \leq 1$). The brightness of a pixel corresponds to the concentration of the tissue in the corresponding

²A voxel is a volume element, representing a value on a regular grid in three-dimensional space. This is analogous to a pixel, which represents 2D image data.

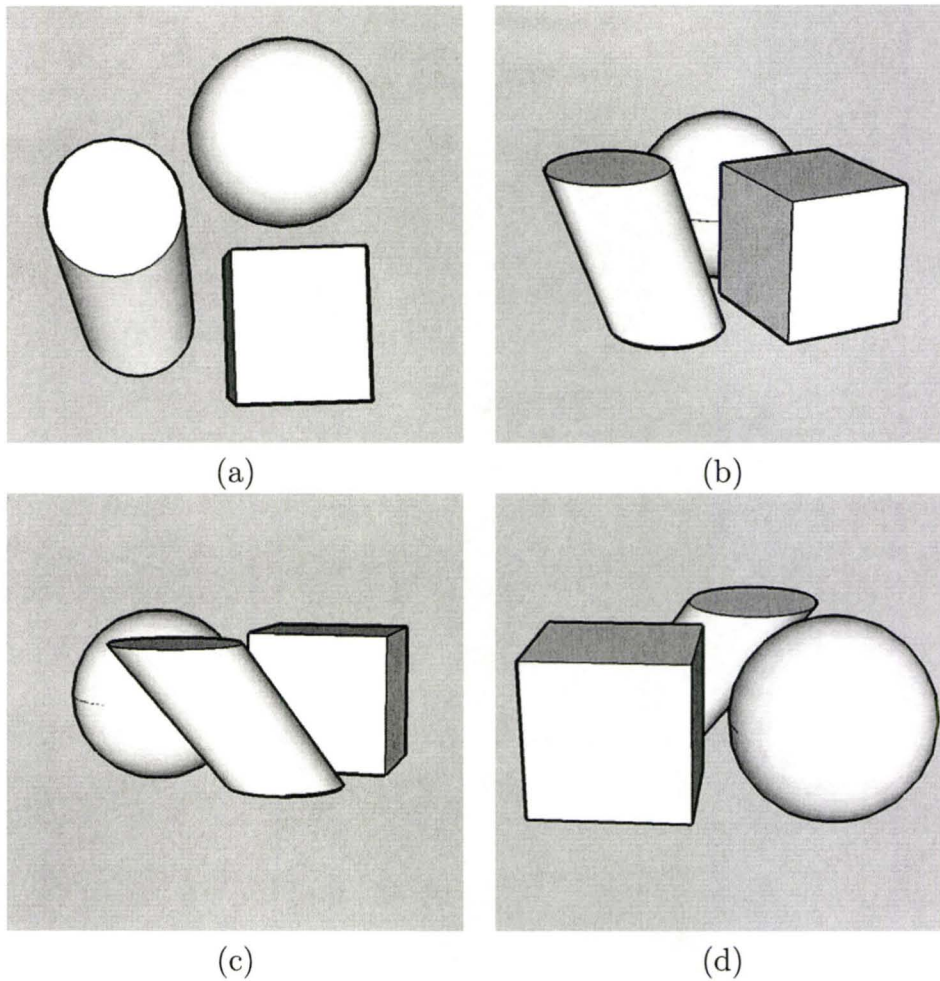


Figure 6.2: 3D view of simulated tissues from different angles (a) top view (b)-(d) side view.

voxel. In our experiments we used an image size of 128×128 and divided voxels into units of $10 \times 10 \times 30$. Figure 6.4 shows a flattened layer of tissue used for MR experiments.

Our algorithm works on multiple MR images acquired from one similar

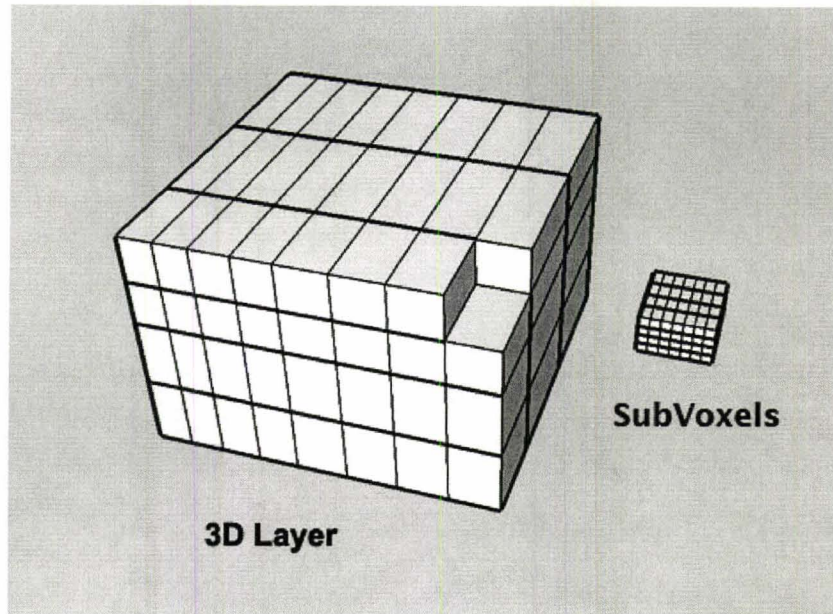


Figure 6.3: A 3D view of a layer of body, divided into voxels. The structure of the top right voxel is shown separately, divided into subvoxels.

anatomy, but with different patterns of data acquisition. We also added white Gaussian noise with different powers using the `wgn()` function in Matlab, in order to simulate the noisy environment of MRI scanners. Four different experiments are manipulated from the non-noisy fully sampled image in Figure 6.4. We used different patterns of data acquisition for each specific experiment. In the following section, we will present different results of our segmentation algorithm on various experiments. We will also show how the regularization term helps to reduce the noise and artifacts in the reconstructed tissue densities.

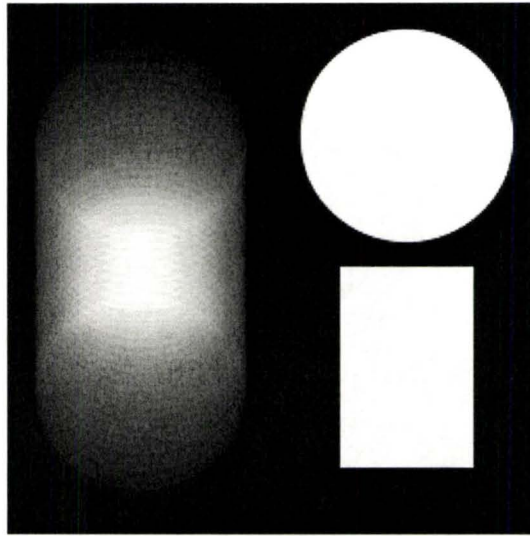


Figure 6.4: Simulated phantom representing flattened MR experiments shown in Figure 6.2.

6.2 Tissue Quantification

Having completely sampled pure tissues, we can manipulate different experiments with different tissue densities using S matrix below. We use 3 distinct tissues containing the effect of partial voluming. Rows in S represents different experiments and columns are different tissues. Considering the geometric shapes in Figure 6.1, the first column corresponds to the sphere, the second column corresponds to the cube, and the third column shows the tissue density of the oblique cylinder. Figure 6.5 (a)-(h) shows the real and imaginary parts of four distinct experiments of size 128×128 , which is used as a base for all our experiments. Segmented tissues also appear in images of size 128×128

separately.

$$S = \begin{pmatrix} 1 + 0i & 1 + 0.15i & 0.8 + 1i \\ 0.25 + 1i & 0 + 0.3333i & 0.4 - 1i \\ 0.325 + 0i & 0.2 + 1i & 0.3 - 0.5i \\ 1 + 0i & 0 + 0.2i & 1 - 1i \end{pmatrix} \quad (6.1)$$

We show reconstructed images under three conditions:

1. Full sampling with zero noise (resulting in reproductions of the model densities).
2. Partial k-space sampling with noise without regularization (resulting in unacceptable noise and artifacts).
3. Partial k-space sampling with noise reconstructed using regularization.

6.2.1 Full Sampling

Segmentation of fully sampled experiments results in reconstruction of pure tissues. Figure 6.5 (i)-(k) shows three tissues with a very clear segmentation.

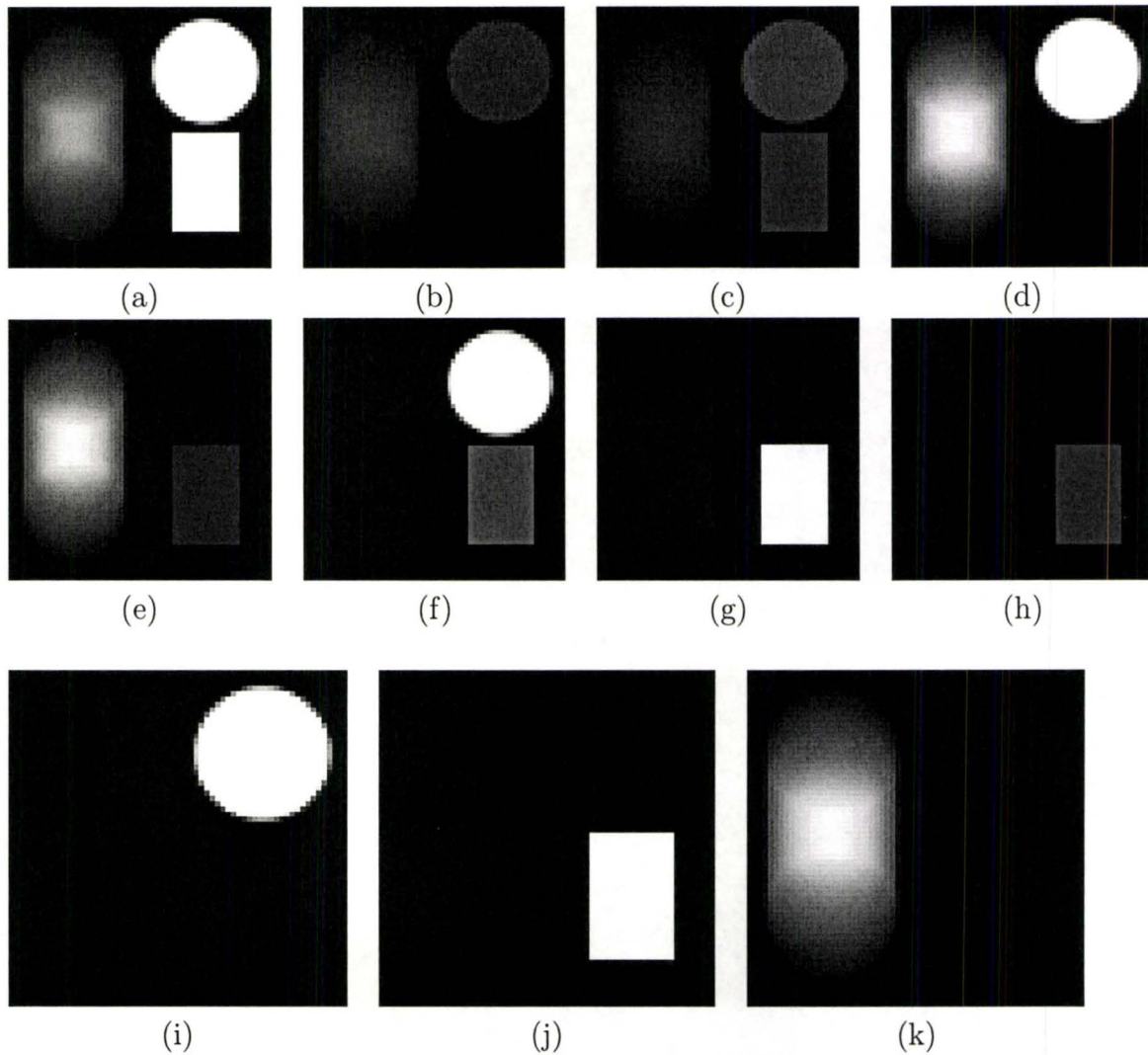


Figure 6.5: Fully sampled experiments are simulated using the Bloch equations from pure tissues as shown in Figure 6.4 using the S transformation. (a)-(d) is the real part and (e)-(h) is the imaginary part of the experiments, (i)-(k) is the quantified tissues from fully sampled MR experiments.

In order to make the phantoms more realistic, we added white Gaussian noise to all experiments. The Matlab function $\text{wgn}(m, n, p)$ creates an 2D array of size $m \times n$ relative to p that indicates the power. By adding the noise to both real and imaginary parts of k-space, we will obtain noisy experiments as shown in Figure 6.6 (a)-(h). The noise is being added to the experiments as follows:

$$\text{expNoise}_i = \text{ifft}(\text{fft}(\text{exp}_i) + \text{wgn}(n, n, p) + i * \text{wgn}(n, n, p)) \quad (6.2)$$

where $\text{fft}()$ and $\text{ifft}()$ are Fourier and inverse Fourier transform functions. Results show that the segmentation is acceptable for experiments with slight noise in Figures 6.6 and 6.7, but adding noise with more power causes unclear segmentation with artifacts in the results as shown in Figure 6.8.

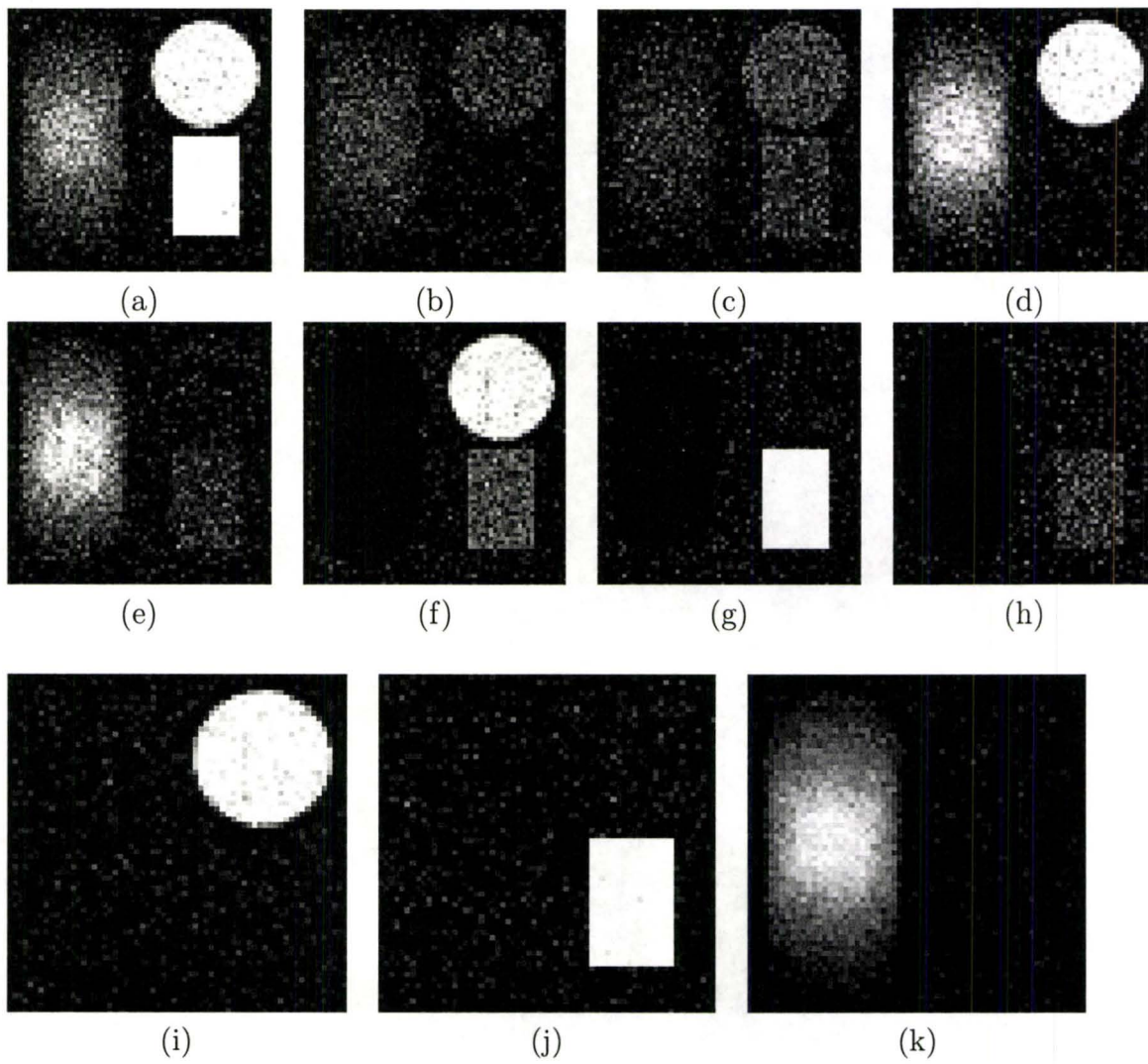


Figure 6.6: Fully sampled experiments contaminated by white Gaussian noise with low power $p = 0.1$ and its corresponding quantification. (a)-(d) is the real part and (e)-(h) is the imaginary part of the experiments. (i)-(k) is the segmented tissues from fully sampled noisy MR experiments.

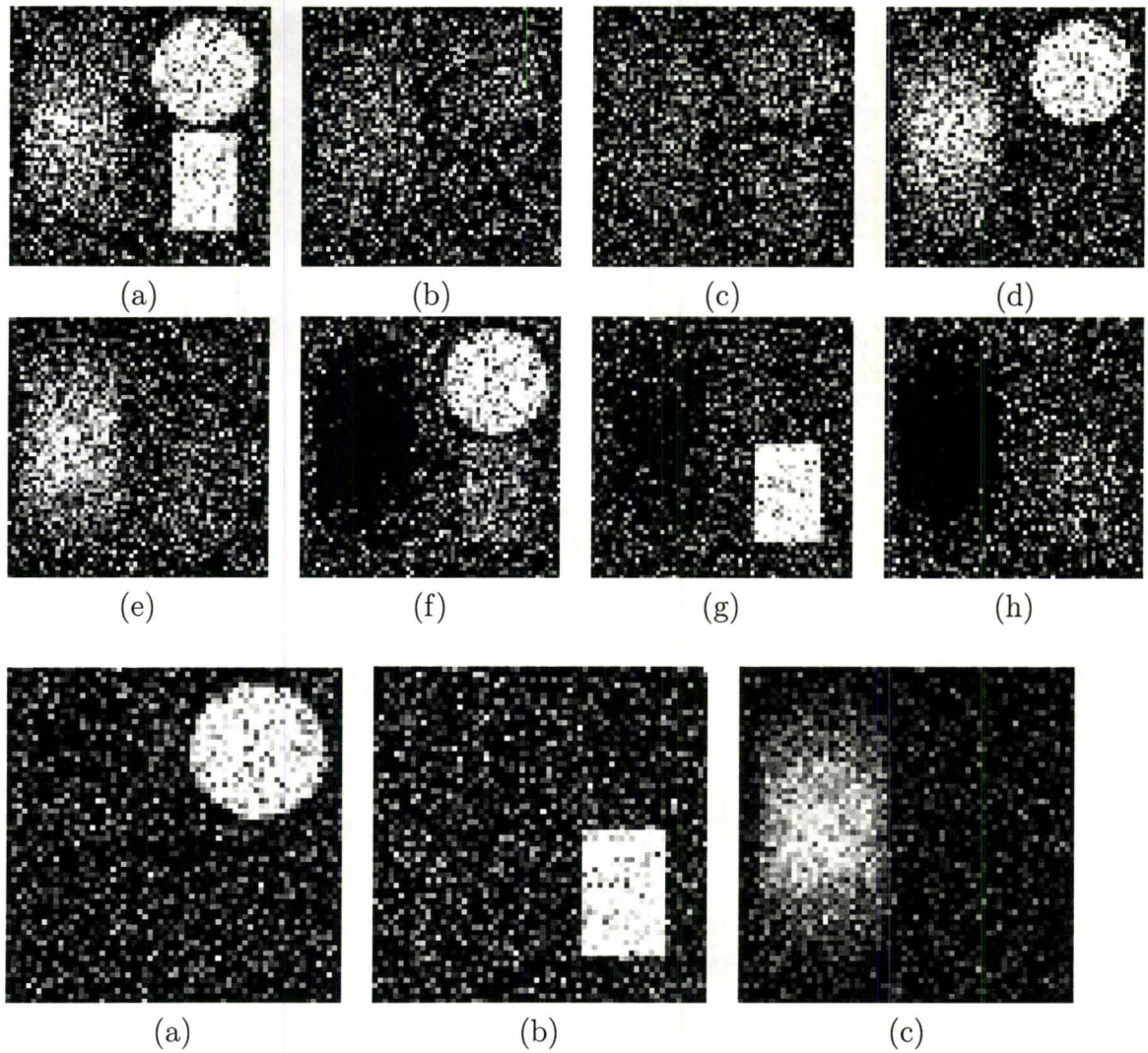


Figure 6.7: Fully sampled experiments contaminated by stronger white Gaussian noise with higher power $p = 10$ and its corresponding quantification which, (a)-(d) is the real part and (e)-(h) is the imaginary part of the experiments, and (i)-(k) is the segmented tissues from fully sampled noisy MR experiments.

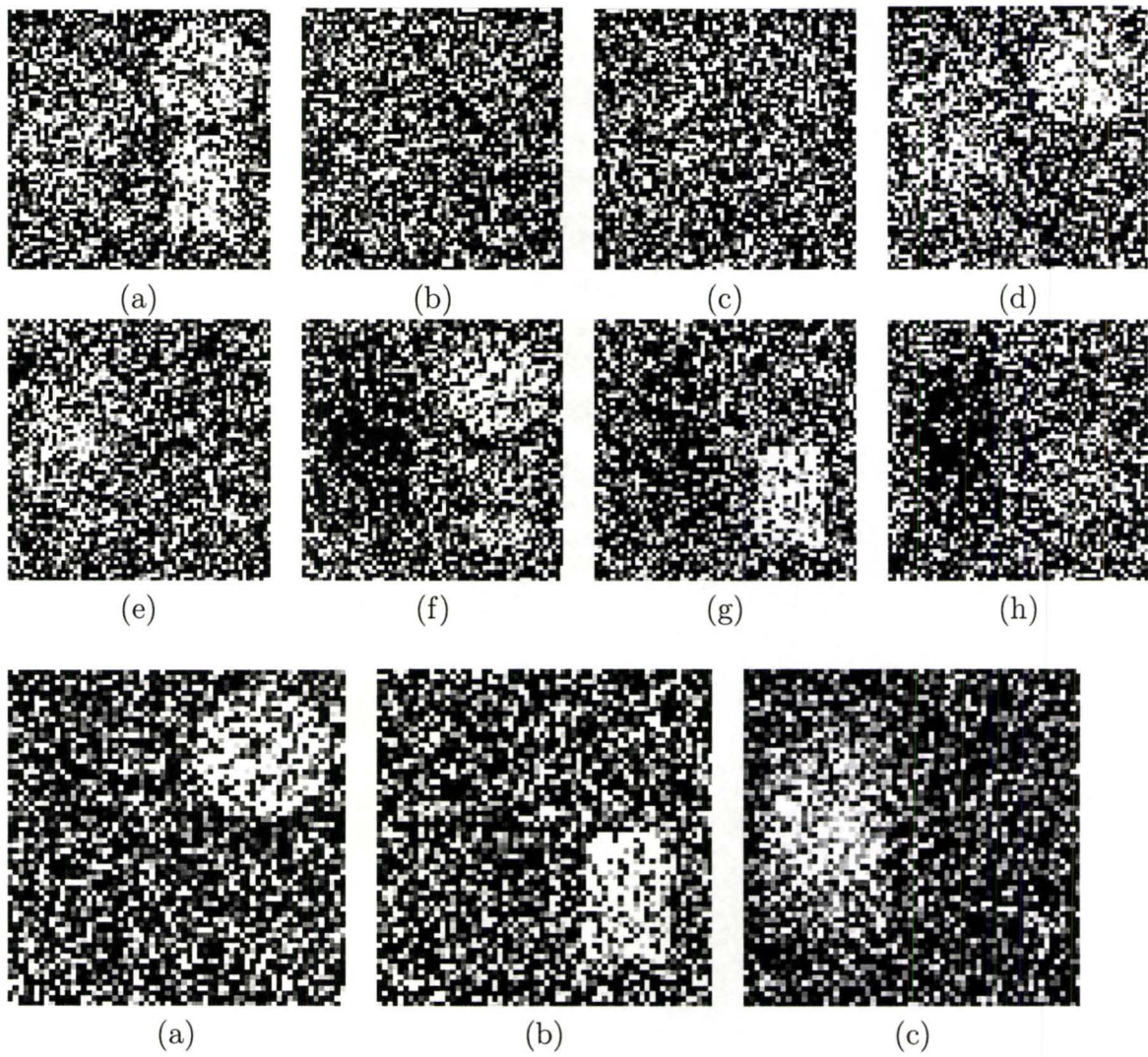


Figure 6.8: Fully sampled experiments contaminated by higher white Gaussian noise with higher power $p = 20$ and its corresponding quantification, which is not clear and contains lots of noises. (a)-(d) is the real part and (e)-(h) is the imaginary part of the experiments. (i)-(k) is the segmented tissues from fully sampled but very noisy MR experiments.

6.2.2 Quantification From Partially Sampled Data (Without Regularization)

In the previous section, we used the fully sampled experiments and showed how noisy data can ruin the segmentation result. In this section, we will present the image reconstruction from incomplete data (partial k-space). In each figure, the sampling used is listed in the corresponding table. Each figure uses a different sampling pattern. We decrease the number of sampled rows in each subsequent figure. Results show that having both noisy and incomplete data, the segmentation is erroneous. Regularizing image segmentation is the approach applied to mitigate the aliasing problem which is presented the next section. For all noisy experiments and their segmentation, we also calculate the Signal to Noise Ratio (SNR) as follows:

$$SNR = \frac{1}{\text{error}}$$

where

$$\text{error} = \sum_{i \in \text{pixels}} \frac{(\text{norm}(\rho_i - \rho_{i,\text{estimate}}))^2}{n^2}$$

where the image size is $n \times n$ and ρ_i and $\rho_{i,\text{estimate}}$ are the basis for segmentation and result of noisy experiment segmentation respectively. Note, the eigenvalues of S^*S give a lower bound on the SNR, but both regularization and the interaction between test problem geometry and sampling patterns may increase the SNR.

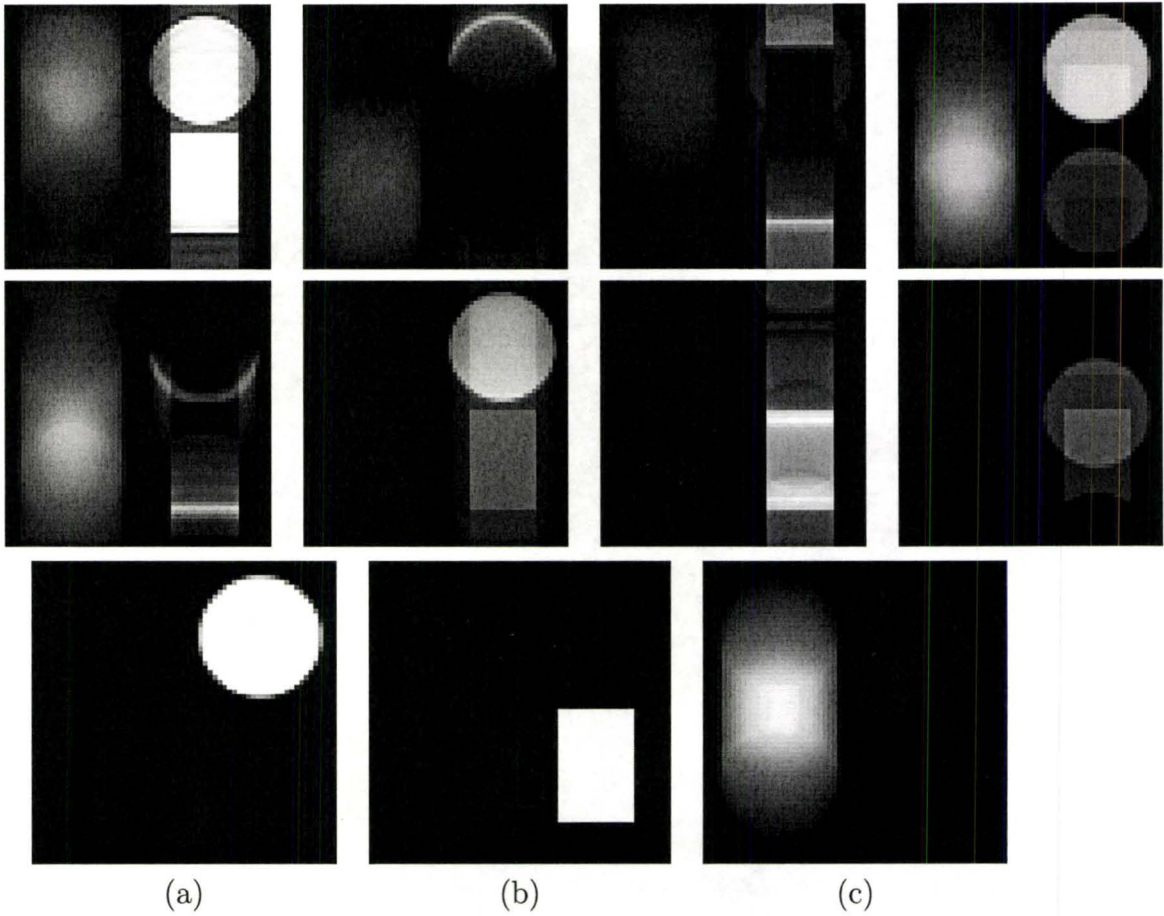


Figure 6.9: Segmented tissues from partially sampled non-noisy MR experiments with mapping shown in Table 6.2.2. The first two rows of the figure are the real and imaginary parts of the experiments, (a)-(c) are the segmented tissues from partial k-space. 58% of complete data was used. The results are without artifacts.

Experiment	Collected Rows in k-space
1	$(1, 2, 3, \dots, \frac{3}{4}n)$
2	$(1, 2, 3, \dots, \frac{1}{2}n)$
3	$(1, 4, 7, 10, \dots, n)$
4	$(1, 2, 3, 5, 6, 7, 9, 10, 11, 13, \dots, n)$

Table 6.1: Sampling of rows from k-space of experiments shown in Figure 6.9.

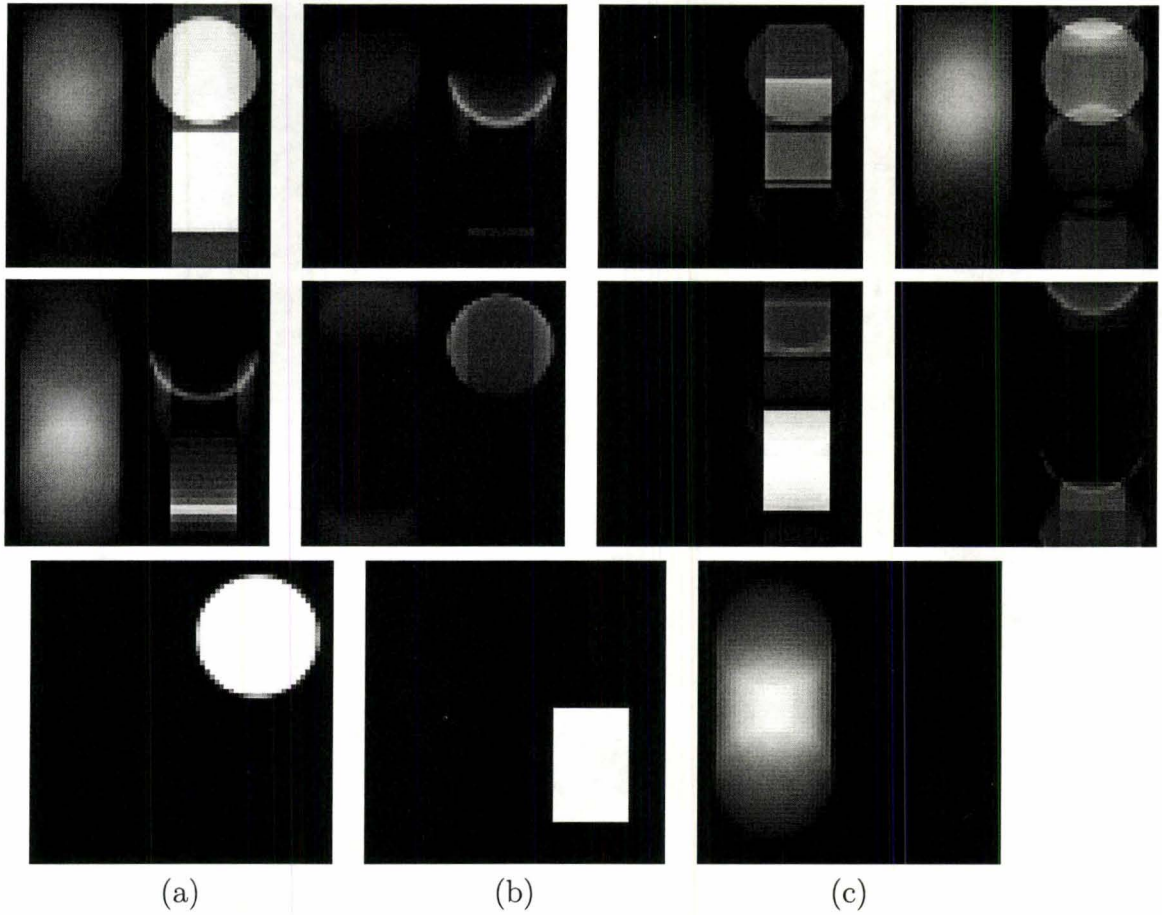


Figure 6.10: Segmented tissues from partially sampled non-noisy MR experiments with mapping shown in Table 6.4. The first two rows of the figure are the real and imaginary parts of the experiments, (a)-(c) is the segmented tissues form partial k-space. 48% of complete data was used.

Experiment	Collected Rows in k-space
1	$(1, 2, 3, \dots, \frac{1}{2}n)$
2	$(\frac{1}{2}n, \dots, n)$
3	$(1, 2, 3, 5, 6, 7, 9, 10, 11, 13, \dots, n)$
4	$(1, 4, 7, 10, \dots, n)$

Table 6.2: Sampling of rows from k-space of experiments shown in Figure 6.10.

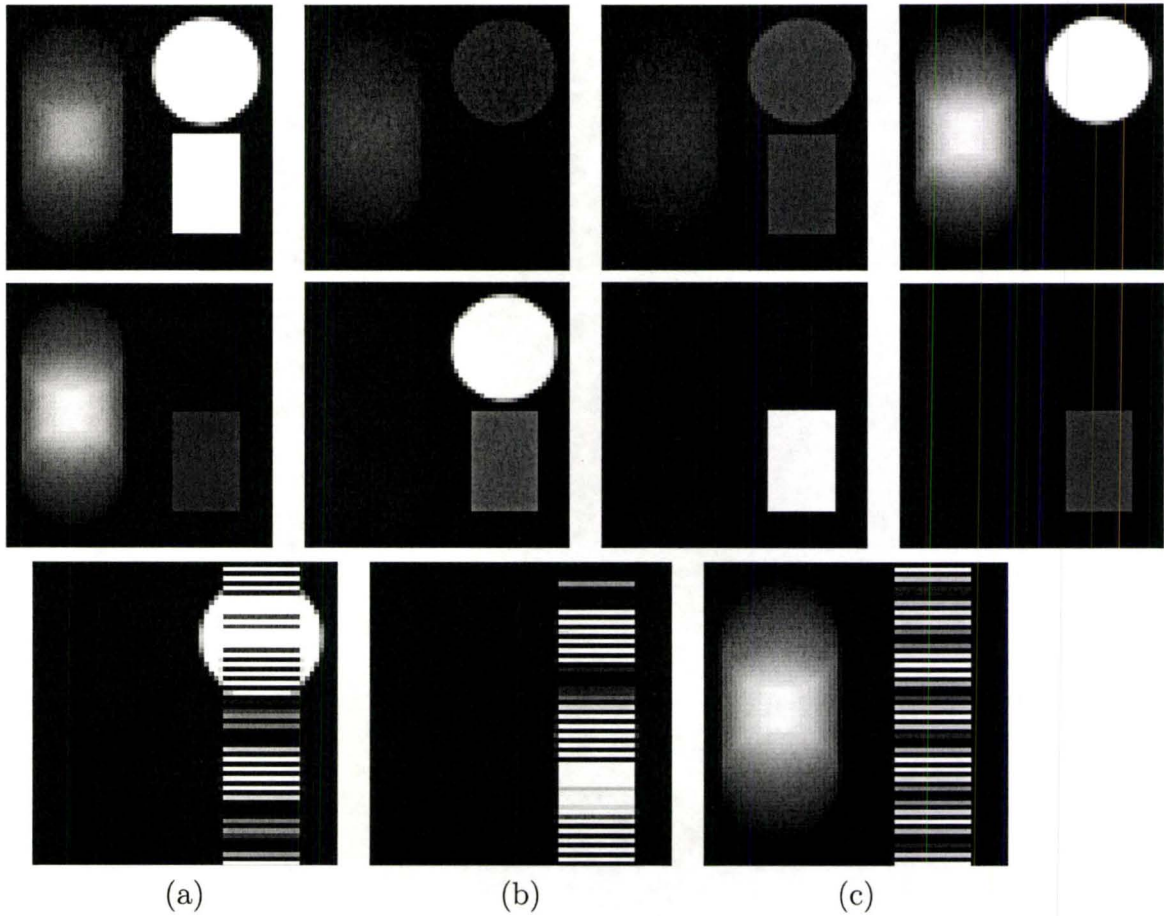


Figure 6.11: Segmented tissues from partially sampled non-noisy MR experiments with mapping shown in Table 6.3. The first two rows of the figure are the real and imaginary parts of the experiments, (a)-(c) is the segmented tissues from partial k-space. 39% of complete data was used.

Experiment	Collected Rows in k-space
1	$(2, 4, 6, \dots, n)$
2	$(1, 2, \dots, \frac{1}{2}n)$
3	$(1, 4, 7, 10, \dots, n)$
4	$(4, 8, 12, 16, \dots, n)$

Table 6.3: Sampling of rows from k-space of experiments shown in Figure 6.11.

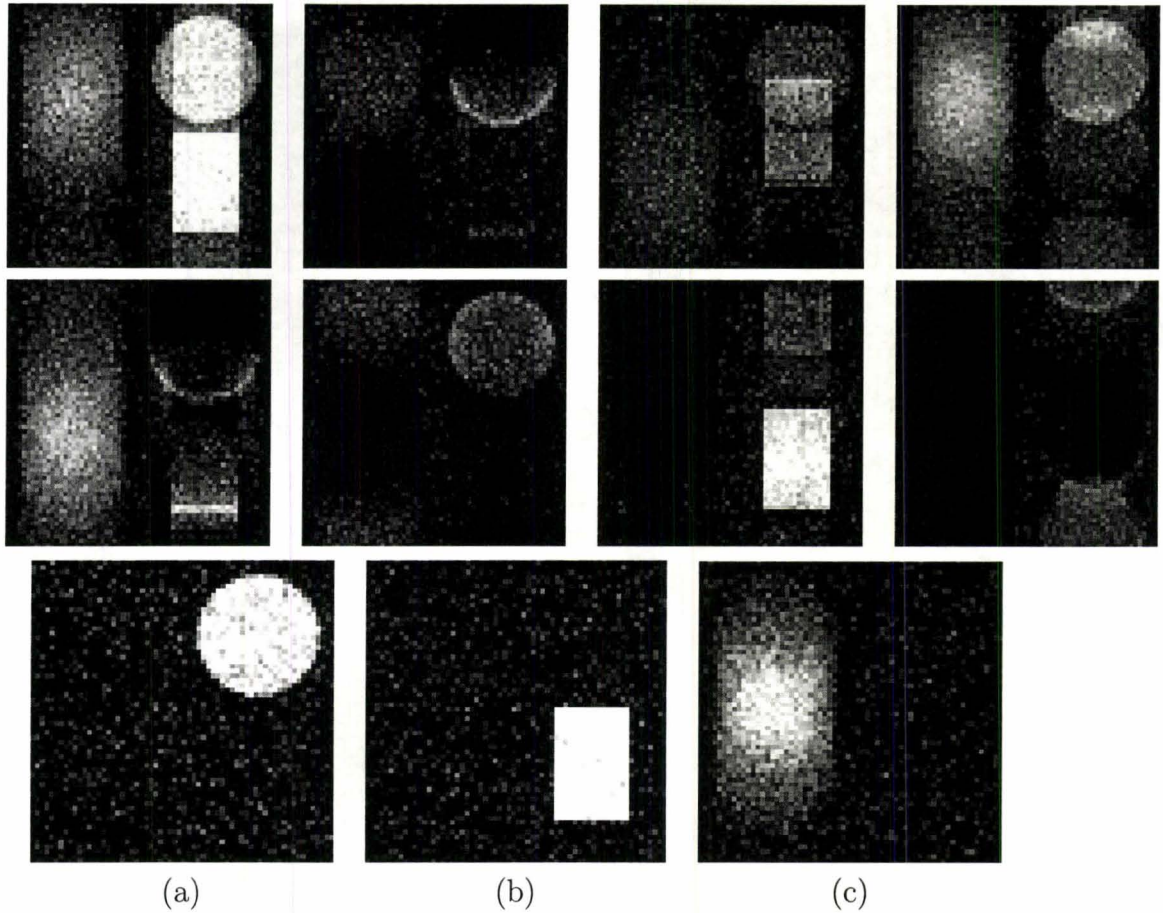


Figure 6.12: Segmented tissues from partially sampled noisy MR experiments with mapping shown in Table 6.4. The first two rows of the figure are the real and imaginary parts of the experiments, (a)-(c) is the segmented tissues from partial k-space. 48% of complete data was used. The results are still fine in spite of having noise.

Experiment	Collected Rows in k-space
1	$(1, 2, 3, \dots, \frac{1}{2}n)$
2	$(\frac{1}{2}n, \dots, n)$
3	$(1, 2, 3, 5, 6, 7, 9, 10, 11, 13, \dots, n)$
4	$(1, 4, 7, 10, \dots, n)$

Table 6.4: Sampling of rows from k-space of experiments shown in Figure 6.12.

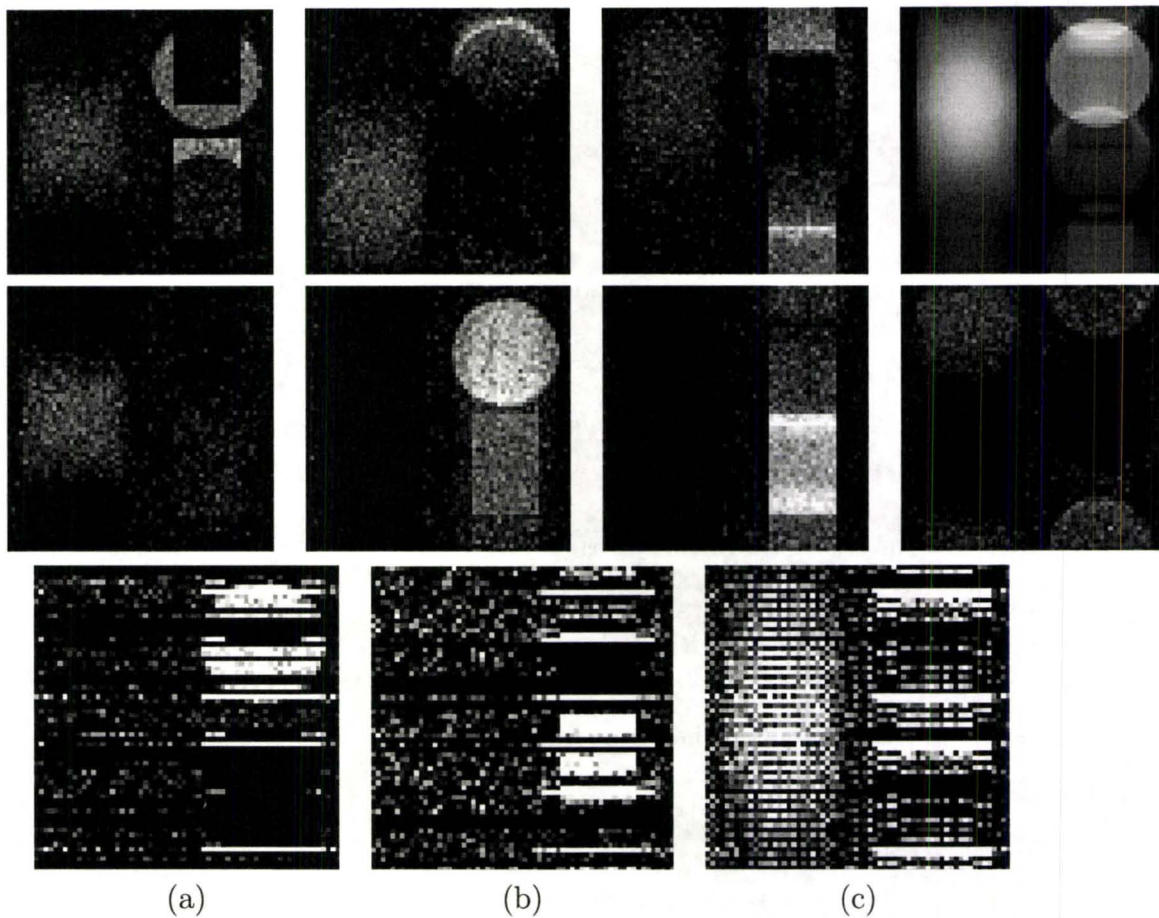


Figure 6.13: Segmented tissues from partially sampled noisy MR experiments with mapping shown in Table 6.3. The first two rows of the figure are the real and imaginary parts of the experiments, (a)-(c) is the segmented tissues from partial k-space. 39% of complete data was used. Having noise and incomplete data, the segmentation result is full of noise and includes artifacts. We need to add a regularizer to change the problem.

6.2.3 Partial k-Space Sampling with Noise Reconstructed Using Regularization

In the previous section, we showed that undersampling of noisy experiments causes aliasing and unwanted artifact in the results (Figure 6.13 (a)-(c)). In this section, we regularize the problem in order to get smoother results with less noise. Later we use the L-curve method to pick a good regularization weight. In Figure 6.17 we compare the three different results. Figure 6.17 (a)-(c) is the unregularized segmentation from noisy data. Figure 6.17 (d)-(f) is the regularized quantification when $\alpha = 1$. Finally, Figure 6.17 (g)-(i) shows the weighted regularized quantification with regularization parameter $\alpha = 3.5$. In the end we will show the L_2 norm of residual as a graph showing the lower error in the results with regularization.

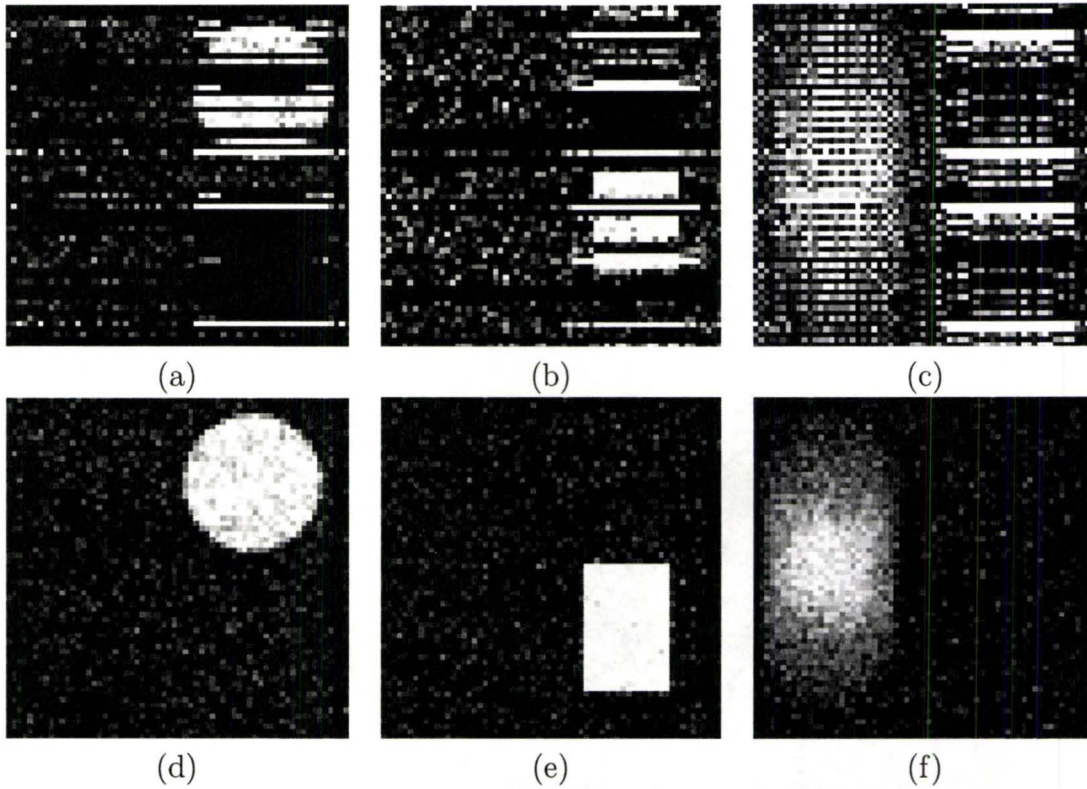


Figure 6.14: Segmentation of partially sampled experiments. Using unweighted regularization ($\alpha = 1$) in both row and column direction improves the noise, especially in the background, removes the artifacts, and also adds a bit of smoothness to the segmented tissues. (a)-(c) are segmentation without regularization ($\alpha = 0$), (d)-(f) are the segmentation of the same tissue using unweighted ($\alpha = 1$) regularization.

6.2.4 L-curve

In order to select the best regularization parameter α , we use the L-curve to find a good compromise. In the previous section, the regularization term improved the results by reducing the artifacts and background noise. The regularization parameter used before was $\alpha = 1$. We can apply different

weightings to α within a certain range of data. If α is very big, we will get over-smoothed results, and if it is very small, the results will look under-smoothed. An over-smoothed image reduces the noise, but doesn't show the details such as edges and contrasts. Figure 6.15 shows over-smoothing and under-smoothing in segmentation.

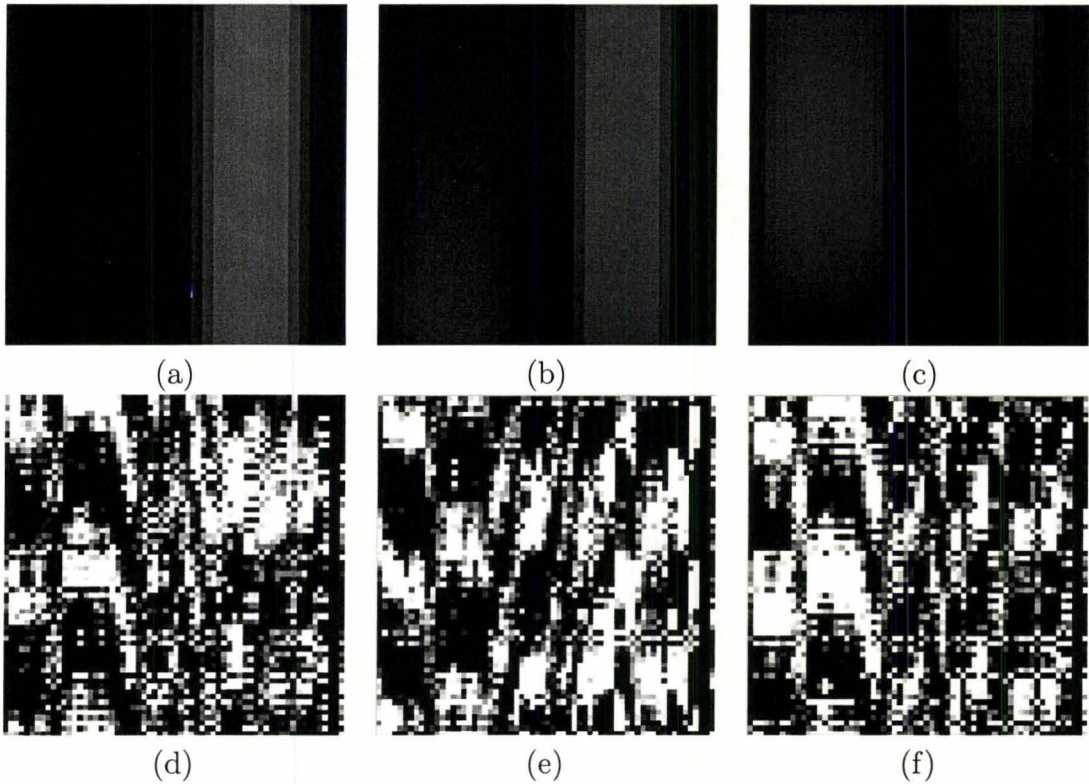


Figure 6.15: Choosing very big or very small α causes over-smoothing and under-smoothing respectively. (a)-(c) are over-smoothed tissues, (d)-(f) are under-smoothed tissues.

We can defined a bounded range of data $[A, B]$ and try to solve the problem for all $\alpha \in [A, B]$. We set the regularization parameter as follows:

$$\alpha = (\sqrt{2})^i, i = -10, \dots, 10$$

By changing α_i in $\|Ax - b\|_2^2 + \alpha_i \|Rx\|_2^2$ we will get different solutions x_{α_i} . Each x_{α_i} can be used to find the trade-off between the fit-to-data term and the regularization term:

$$(\|Ax_{\alpha_i} - b\|_2, \|Rx_{\alpha_i}\|_2)$$

By using the L-curve technique, we can find a good trade-off α which is located at the very left of the curvature shown in Figure 6.16, e.g. $\alpha = 3.5$. Figure 6.17 (g)-(i) show the weighted regularization with better and more smooth results.

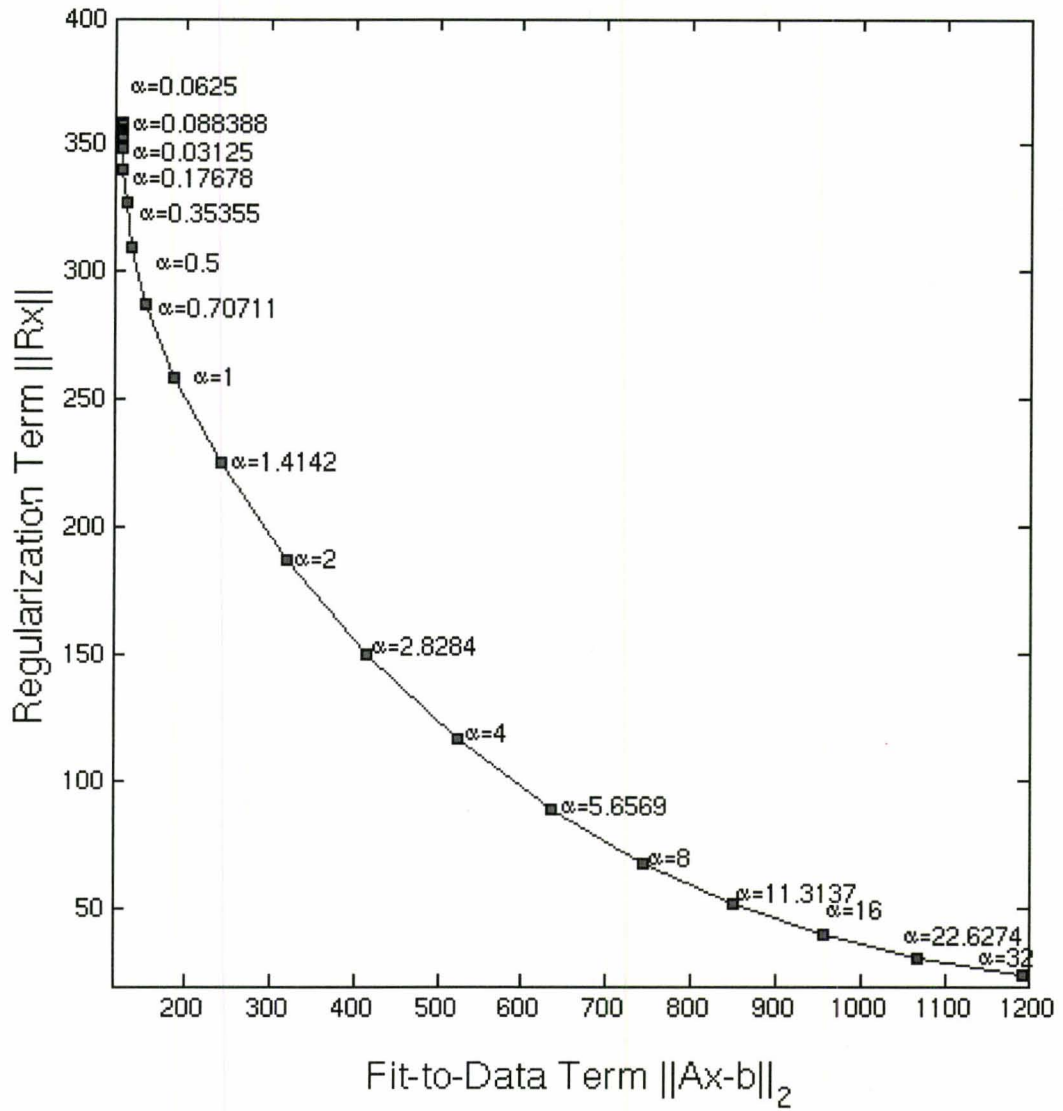


Figure 6.16: L-curve (zoomed-in by using a linear-linear scale).

6.2.5 Standard Deviation of Noise

Finding a good regularization parameter is one of the criteria for having the visually best results. However, we can also calculate the error in the segmented

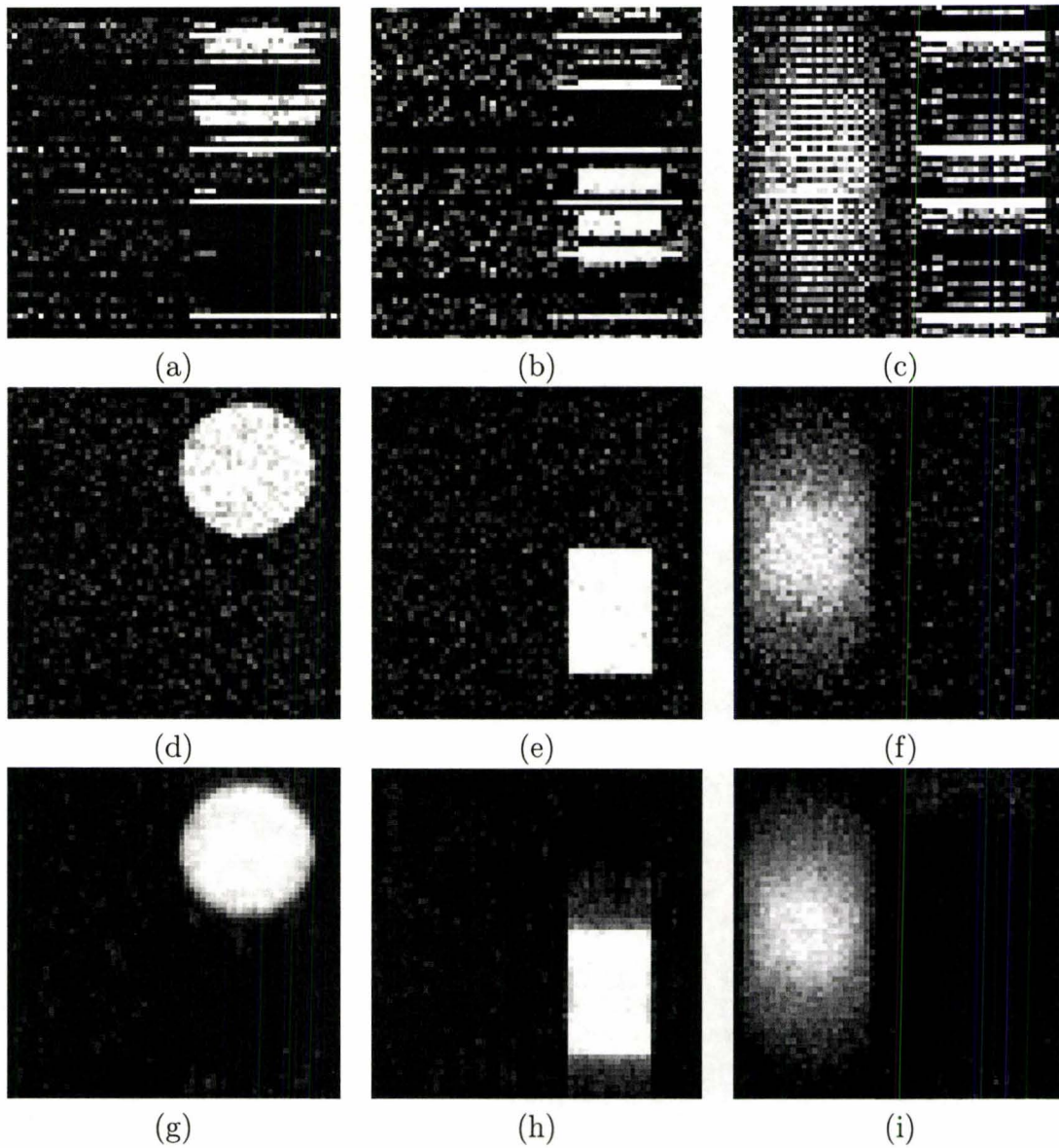


Figure 6.17: A comparison between different segmentations applied on the same partially sampled experiment with sampling patterns shown in 6.3 and with the same amount of noise. We obtained better segmentation results using weighted regularization. (a)-(c) is an unregularized segmentation ($\alpha = 0$), (d)-(f) is the segmentation using unweighted regularization ($\alpha = 1$), (g)-(i) is the regularized tissue segmentation with regularization parameter ($\alpha = 3.5$). Only using 39% complete data used for image reconstruction. Table 6.2.4 shows the SNR of the segmented tissues.

Experiment	Tissue1	Tissue2	Tissue 3
Tissues (a)-(c)	1.7327	2.9124	1.32870
Tissues (d)-(f)	105.6959	31.7963	151.3333
Tissues (g)-(i)	110.2940	35.1466	157.0307

Table 6.5: Signal to Noise Ratio (SNR) related to segmented tissues shown in Figure 6.17 with the same order as tissues are presented.

image caused by incomplete data sampling and noise. We can consider the pure and non-noisy tissue shown in Figure 6.5 (i)-(k) as a basis and compare it to our results. Standard deviation is a measure of how spread out the data are compared to a basis. If there are n different images, the standard deviation S_n is defined as:

$$S_n = \sqrt{\sum_{i \in pixels}^n (x_i - \bar{x}_i)^2} \quad (6.3)$$

where \bar{x} is the basis (pure tissue).

Table 6.6 shows the standard deviation of the noise in our segmented images. Results show that using weighted regularization decreases the L_2 norm of residual error.

Segmented Image	$\ residual\ _{L2}$
Full k-space, No Noise	0
Full k-space with Noise, $\alpha = 0$	6.4397
Partial k-space With Noise, $\alpha = 0$	13.995
Regularized Image, $\alpha = 1$	5.561
Regularized Image, $\alpha = 3.5$	4.556

Table 6.6: Standard deviation of results of different problems.

6.2.6 Execution Time

All tests were performed on Power Mac G5 which contains the PowerPC 970 (2.2) Dual CPU and 2 GB of RAM. Matlab version 7.0.4.352(R14) was used. Table 6.7 shows the execution time as a function of problem size. When k-space is fully sampled, the A in fit-to-data term has the maximum size. Where k-space is partially sampled, the A would be smaller because we remove the rows to prevent singularity of matrix. Results show that the elapsed time increases by increasing the size and number of images.

Experiment Size	Elapsed Time (s)	Elapsed Time (min)
16×16	0.979	0.016
32×32	10.55	0.17
64×64	109.171	1.8
128×128	935.524	15
256×256	38230.05	637

Table 6.7: Regularized segmentation. Execution time increases by increasing the size of the image.

Chapter 7

Conclusion and Future Work

7.1 Conclusion

We have formulated tissue quantification from multiple MR images with different contrasts as an inverse problem. We have shown that incomplete k-space sampling may introduce random and structured noise in the reconstructed tissue fractions, although the results of solving one inverse problem are better than the results obtained by reconstructing the images separately and doing the quantification pixel by pixel. Further reduction in apparent noise results from using the Tikhonov-Phillips regularization as part of the inverse problem. This also reduces noise in the quantification, when the simulated data contains significant noise. In the regularized case, we were able to undersample experiments in order to save 61% of the full scan time, without introducing noticeable artifacts. The improvements in image quality were reflected in standard measurements of SNR.

7.2 Future Work

The next steps in developing this method are to (1) construct a phantom with known materials and geometry in order to validate the method, and (2) develop a method of determining tissue properties (i.e. the S transformation) rapidly, either using the collected data or preliminary low-resolution images, and new or existing machine learning algorithms (e.g. k-means or more sophisticated methods using support vector machines).

The most successful partial k-space technique for reducing acquisition time is Sensitivity encoding (SENSE). SENSE is based on the fact that receiver sensitivity generally has an encoding effect complementary to Fourier preparation by linear field gradients. Thus, by using multiple receiver coils in parallel, scan time for Fourier imaging can be considerably reduced. The problem of image reconstruction from sensitivity-encoded data is formulated in a general fashion and solved for arbitrary coil configurations and k-space sampling patterns. In the future, the methods of this paper should be combined with SENSE for even greater reductions in acquisition time.

We used the linear least-squares function in Matlab to solve the problem. However, by using techniques such as Conjugate Gradient, we will be able to solve larger problems. Tikhonov regularization was successful. However, we should also try different regularization methods such as Total Variation, which have shown themselves to be even better on related imaging problems.

Appendix A: The Matlab Codes

A.1 Function imgSegRealRegMultiCol2.m

```
function [Rho]=imgSegRealRegMultiCol2(exp, S, projection, rho, alpha)
%-----
%exp:    The cell of experiments. Each element of exp
%        (e.g. exp{1}) contains an MR experiment of size n*n
%S:      A tranformaton from tissue density to pixle value
%rho:    The number of tissues to be segmented
%alpha:  Regularization parameter
%Rho:    A cell which contains the segmented tissues
%-----

%% Variable Assignment
n=size(exp{1},1);    %Image Size
e=size(exp,1);      %Number of Expriments
t=rho;              %Number of Tissues
Rho=cell(t,1);      %Declaring output Varibale
Bcell=cell(e,1);
piCell=cell(e,1);
p_ftCell=cell(e,1);
c=4;                %Number of Columns processed at each iteration
step=2;             %Step Size Used In Regularization

%% Making Sample Projection Matrix pi and Remove the Zero Rows

%Finding the error rows in Projection Matrix
ProTemp=projection;
tempA=[1:n];

for i=1:e
```

```
projection{i}=tempA;
projection{i}(ProTemp{i})=[];
piCell{i}=eye(2*n);

%removing zero rows from each projection matrix
if (size(projection{i},2) ~= 0)
    index=[2*projection{i}-1 , 2*projection{i}];
    piCell{i}(index,:)=[];
end%end if

end

%% make nxn matrix of 1D Fourier Transform for Real Computation

FT = makefftReal(n); %Makes 2n x 2n Real Fourier Matrix

%% Making a Block Digonal P_FTp With Blocks of (P*FTp)

P_FTp=[];

for i=1:e
    P_FTp=blkdiag(P_FTp,piCell{i}*FT);
end

%% Making Sp, a Diagonal Matrix Which Is a Transformation From from tis:
% densiies to pixel values.

Scell=cell(t,1);
SpCell=cell(e,1);
Sp=[];

for i=1:e;
    Scell{i}=S(i,:);
    for j=1:t
        block=[real(Scell{i}(j)); imag(Scell{i}(j))];
        SpCell{i}= horzcat(SpCell{i}, blockDiagonal(n,block));
    end
    Sp=vertcat(Sp,SpCell{i});
end

end
```

```
% Building Variable for Solver A,b in ||A.x-b||

A=P_FTp*Sp;
A_Block=[];
for i=1:c
    A_Block=blkdiag(A_Block,A);
end

expReal=cell(e,1);
for i=1:e
    expReal{i}=makeReal(exp{i});%separate the real and imaginary part of
                                %the image and put them together in
                                %2n x 2n matrix
end

for i=1:e
    Bcell{i} = piCell{i}*FT*(expReal{i});
end

% Building Tikhonov Regularization matrix

TikhvReg=eye(t*n)+diag(-1*ones(t*n-1,1),1);

Tikhv_Col=[];

for i=1:c
    Tikhv_Col=blkdiag(Tikhv_Col,TikhvReg);
end
leftBlock=[];
rightBlock=[];
for i=1:c-1
    leftBlock=blkdiag(leftBlock,eye(t*n));
    rightBlock=blkdiag(rightBlock,-1*eye(t*n));
end
leftBlock=horzcat(leftBlock,zeros(t*n*(c-1),n*t));
rightBlock=horzcat(zeros(t*n*(c-1),n*t),rightBlock);
Tikhv_Row=(leftBlock+rightBlock);
```



```
A_Reg=vertcat(A_Block,alpha*Tikhv_Col,alpha*Tikhv_Row); %A in least square  
  
%% Solving Linear Least Squares  
  
options = optimset('LargeScale', 'on','Display', 'iter');  
col=1;  
  
for j=1:step:n-2  
    b=[];  
    for k=j:(j-1)+c  
        for i=1:e  
            b=vertcat(b,Bcell{i}(:,k));  
        end%for i  
    end%for k  
  
b=vertcat(b,zeros(c*n*t,1),zeros((c-1)*n*t,1));  
  
    [Rhos(:,col)] = lsqlin(A_Reg,b,[],[],[],[],[],[],[],[],'options');  
    col=col+1;  
end  
  
%% Making Output Figure  
  
Rhos(:,col)= zeros(size(A_Reg,2),1);  
reshapedRhos=Rhos(1:n*t,1);  
  
for i=2:(n/step)  
    temp=Rhos( (n*t)+1:3*n*t,i);  
    reshapedRhos=vertcat(reshapedRhos,temp);  
end;%for i  
reshapedRhos=vertcat(reshapedRhos,Rhos(3*(n*t)+1:4*n*t,n/step-1));  
  
for j=1:n  
    %read a column which contains j'th column information of all t tissues  
    column=reshapedRhos((j-1)*t*n +1:t*n*j,1);  
    for i=1:t  
        Rho{i}(:,j)=column( (i-1)*n+1 : i*n,1);  
    end;%for i  
  
end%end j
```

```
%% Plotting The Segmented Results

figure(1); clf;

set(gcf, 'Position', [400 600 1000 800]);

i=3;
j=4;
offset=4;

subplot(i,j,1); imshow(abs(real(exp{1}))); title('Experiment1 Real Part');
subplot(i,j,1+offset);imshow(abs(imag(exp{1}))); title('Experiment1 Imagina:

subplot(i,j,2); imshow(abs(real(exp{2}))); title('Experiment2 Real Part');
subplot(i,j,2+offset);imshow(abs(imag(exp{2}))); title('Experiment2 Imagina:

subplot(i,j,3); imshow(abs(real(exp{3}))); title('Experiment3 Real Part');
subplot(i,j,3+offset);imshow(abs(imag(exp{3}))); title('Experiment3 Imagina:

subplot(i,j,4); imshow(abs(real(exp{4}))); title('Experiment4 Real Part');
subplot(i,j,4+offset);imshow(abs(imag(exp{4}))); title('Experiment4 Imagina:

subplot(i,j-1,7); imshow(real(Rho{1})); title('Segmented Tissue1');
subplot(i,j-1,8); imshow(real(Rho{2})); title('Segmented Tissue2');
subplot(i,j-1,9); imshow(real(Rho{3})); title('Segmented Tissue3');
```

A.2 Function makeShape.m

```
function [img1,img2,img3]=makeShape(n)
%-----
%This function make 3 different geometric phantoms of size n * n
%n:           The size of image
%Img1,Img2,Img3:   Built Tissues
%-----
%% variables

l=10;           %Length of Layer
w=10;           %Width of Layer
h=30;           %Hight of Layer
```

```
img1=zeros(n);
img2=zeros(n);
img3=zeros(n);
centerE=[2*(n/8)*w,6*(n/8)*l,0];
rE=n/5*l;

%% Bulid an Sphere

offesetjj=1;
offsetii=1;
%we process each voxel separately, we try to sum up the sub voxel of eac
%voxel which are part of our shape

for i=1:n      % i goes in row direction
    for j=1:n % j goes in column direction
        sum=0;
        for kk=0:h % voxel hight
            for jj=offesetjj:w+offesetjj-1 %voxel col

                for ii=offsetii:l+offsetii-1 % voxel row

                    dist=sqrt( (ii-centerE(1))^2 + (jj-centerE(2))^2
                    if (dist<=rE)
                        sum= sum+ 1/(l*w*h);
                    end% end if

                end%for ii
            end%for jj
        end%for kk

        if (sum~=0)
            img1(i,j)=sum;
        end;
        offesetjj=offesetjj+w;
    end%for j
    offesetjj=1;
    offsetii=offsetii+l;
end%for i
```

```
%% Building Cube

x1C=5*(n/8)*l;
x2C=7*(n/8)*l;

y1C=(n/2)*w;
y2C=7*(n/8)*w;

z1C=0;
z2C=h;

offesetjj=0;
for i=1:n
    offsetii=0;
    offesetjj=offesetjj+w;

    for j=1:n
        sum=0;
        for kk=0:h
            for jj=offesetjj:w+offesetjj

                for ii=offsetii:l+offsetii

                    dist=sqrt( (ii-centerE(1))^2 + (jj-centerE(2))^2 );
                    if ( (x1C<=ii)& (ii<=x2C) &(y1C<=jj) && (jj<=y2C) & ...
                        (z1C<=kk) & (kk<=z2C) )
                        sum= sum+ 1/(l*w*h);
                    end% end if
                end%for ii
            end%for jj
        end%for kk

        if (sum~=0)
            img2(i,j)=sum;
        end;

        offsetii=offsetii+l;
    end%for j
end%for i
```

```
% Building Oblique Cylinder

C1 = [n/4*1,2*n/8*w,0];
C2 = [n/4*1,6*n/8*w,30];
rC=n/5*1;

syms t;
line = C1 + t*(C2-C1); % line passing middle of inclined cylinder

offesetjj=0;
for i=1:n
    offsetii=0;
    offesetjj=offesetjj+w;

    for j=1:n
        sum=0;
        for kk=0:h
            t=(kk-C1(3))/(C2(3)-C1(3));
            x1=C1(1)+t*(C2(1)-C1(1));
            y1=C1(2)+t*(C2(2)-C1(2));

            for jj=offesetjj:w+offesetjj

                for ii=offsetii:l+offsetii

                    dist=sqrt( ((ii-x1)^2 + (jj-y1)^2 ) );
                    if (dist<=rC)
                        sum= sum+ 1/(l*w*h);
                    end% end if

                    a=2;
                end%for ii
            end%for jj
        end%for kk

        if (sum~=0)
            img3(i,j)=sum;
        end;
        offsetii=offsetii+l;
    end
end
```

```
        end%for j
    end%for i

end
```

A.3 Function makefftReal.m

```
function ft_array = makefftReal(n)
%-----
% creates the real FT array of size 2n x 2n
%-----
ft_array=[];
for k=1:n
    row=[];
    for j=1:n
        if (i==1 || j==1)
            row=horzcat(row,eye(2));
        else
            block=[cos((-2*pi*(j-1)*(k-1))/n) -sin((-2*pi*(j-1)*(k-1))/n);
                  sin((-2*pi*(j-1)*(k-1))/n) cos((-2*pi*(j-1)*(k-1))/n)];
            row=horzcat(row,block);
        end

    end
    ft_array=vertcat(ft_array,row);
end
```


Bibliography

- [1] B. Benoit and R. Chaoui. Three-dimensional ultrasound with maximal mode rendering: a novel technique for the diagnosis of bilateral or unilateral absence or hypoplasia of nasal bones in second-trimester screening for down syndrome. *Ultrasound in Obstetrics and Gynecology*, 25(1):19–24, 2004.
- [2] M. Bertero, T. Poggio, and V. Torre. Ill-posed problems in early vision. *IEEE*, 76(8):869–889, 1987.
- [3] F. Bloch. Nuclear induction. *Phys. Rev*, 460, 1946.
- [4] P. Boesiger and K. Pruessmann. Sense: Sensitivity encoding for fast mri <http://www.mr.ethz.ch>. [Online; accessed 11-March-2008].
- [5] BrainFlux. 2d fft java applet <http://www.brainflux.org/java/classes/FFT2DApplet.html>, 2004. [Online; accessed 01-June-2008].
- [6] D.J. Brenner and E.J. Hall. Computed tomography—an increasing source of radiation exposure. *The New England Journal of Medicine*, 357(22):2277–2284, 2007.
- [7] J.W. Clark. Neural network modeling. *Phys. Med. Biol*, 36:1259–1317, 1991.
- [8] W.T. Dixon. Simple proton spectroscopic imaging. *Radiology*, 153:189–194, 1984.
- [9] J.P. Felmlee, R.L. Morin, and J.R. Salutz. Magnetic resonance imaging phase encoding: a pictorial essay. *Radiographics*, 9(4):717–722, 1989.
- [10] J.P. Gonzalez and U. Ozguner. Lane detection using histogram-based segmentation and decision trees. *Intelligent Transportation Systems*, 10:346–351, 2000.

- [11] E. M. Haacke, R.W. Brown, and M.L. Thompson. *Magnetic Resonance Imaging: Physical Principles and Sequence Design*. John Wiley,, 1st, edition, 1999.
- [12] J. Hadamard. Sur les problmes aux drives partielles et leur signification physique. *Princeton University Bulletin*, 13:49–52, 1902.
- [13] P.C. Hansen. Analysus of discrete ill-posed problems by means of the l-curve. *SIAM Review*, 34(4):561–580, 1992.
- [14] P.C. Hansen. The l-curve and its use in the numerical treatment of inverse problems. *Royal Society Proceedings A*, 461(2063):3525–3542, 2005.
- [15] R.M. Haralick and L.G. Shapiro. Image segmentation techniques. *Computer Vis. Graph. Image Proc*, 29:100–132, 1985.
- [16] J. A. Hartigan and M. A. Wong. A k-means clustering algorithm. *Applied Statistics*, 28(1):100–108, 1979.
- [17] D. M. Higgins. What is k-space? <http://www.revisemri.com>. [Online; accessed 20-April-2008].
- [18] M. Kass and A. Witkin. Snakes: Active contour model. *International Journal of Computer Vision*, 1(4):321–331, 1978.
- [19] M.E. Kilmerd and D.P. OLeary. Choosing regularization parameter in iterative methods for ill-posed problems. *SIAM J Matrix Anal Aappl*, 22(4):1204–1221, 2001.
- [20] K.F. King. Partial fourier acquisition of mr data over a limited field of view and image reconstruction <http://www.patentstorm.us/patents/6242916/claims.html>, 2004. [Online; accessed 11-June-2008].
- [21] C.L. Lawson and R.J. Hanson. *Solving Least Square Problems*. SIAM, Philadelphia, PA, 1st, edition, 1995.
- [22] C. Lee, S. Huh, and T.A. Ketter. Unsupervised connectivity-based thresholding segmentation of midsagittal brain mr images. *Comput Biol Med.*, 28(3):309–38, 1998.
- [23] C.M. Leung and W.S Lu. An l-curve approach to optimal determination of regularization parameter in image restoration. *IEEE*, 10(4):1021–1024, 1993.

- [24] Z.P. Liang and P.C. Lauterbur. Principles of magnetic resonance imaging. *IEEE Press Series in Biomedical Engineering*, 1999.
- [25] S. Ljunggren. A simple graphical representation of fourier-based imaging methods. *Journal of Magnetic Resonance*, 54:338–343, 1983.
- [26] V. A. Morozov. On the solution of functional equations by the method of regularization. *Soviet Math. Dokl*, 7:414–417, 1996.
- [27] D.G. Nishimura. *Principles of Magnetic Resonance Imaging*. Dept. of Electrical Engineering, Stanford University, CA, 1996.
- [28] B. Odom, D. Hanneke, and B. D’Urso. New measurement of the electron magnetic moment using a one-electron quantum cyclotron. *Physical Review Letters*, 97, 2006.
- [29] D.L. Pham, C. Xu, and J.L. Prince. Current methods in medical image segmentation. *Annual Review of Biomedical Engineering*, 2:315–337, 2000.
- [30] Magnetic Resonance Technology Information Portal. Mr-tip-mri images:breast mri images t2 and t1.
- [31] K.P. Pruessmann, M. Weiger, and M.B. Scheidegger. Sense: sensitivity encoding for fast mri. *The New England Journal of Medicine*, 42(5):952–962, 1999.
- [32] T. Ren. An optimal design method for mri teardrop gradient waveforms. Master’s thesis, McMaster University, 2005.
- [33] P.K. Sahoo and S. Soltani. A survey of thresholding techniques. *Computer Vision, Graphics, and Image Processing*, 41(2):233–260, 1988.
- [34] K. Tanabe. Projection method for solving a singular system of linear equations and its applications. *Numer. Math*, 17:203–214, 1971.
- [35] A.N. Tikhonov. Solution of incorrectly formulated problems and the regularization method. *Soviet Math Dokl* 4, 151:501–504, 1963.
- [36] D. Twieg. The k-trajectory formulation of the nmr imaging process with applications in analysis and synthesis of imaging methods. *Medical Physics*, 10(5):610–621, 1983.

- [37] D.B. Twieg. The k-trajectory formulation of the nmr imaging process with applications in analysis and synthesis of imaging methods. *Medical Physics*, 10:610–621, 1983.
- [38] Wikipedia. K-means algorithm http://www.en.wikipedia.org/wiki/K-means_algorithm, 2008. [Online; accessed 12-April-2008].
- [39] Wikipedia. Nuclear magnetic resonance imaging http://en.wikipedia.org/wiki/Magnetic_resonance_imaging, 2008. [Online; accessed 23-May-2008].
- [40] X.J. Xue, K.J. Kozaczek, and S.K. Kurtzl. A direct algorithm for solving ill-conditioned linear algebraic systems. *Advances in X-ray Analysis*, 41:629–633, 2000.
- [41] T.S. Yoo. *Insight into Images: Principles and Practice for Segmentation, Registration, and Image Analysis*. Bar Ilan University Press, Jericho, New York, 1st, edition, 1996.
- [42] Z. Zheng. Magnetic resonance tissue quantification using optimal pulse sequence design. Master’s thesis, McMaster University, 2005.
- [43] B. Zitov and J. Flusser. Image registration methods: a survey. *Image Vision Computing*, 21(11):977–1000, 2003.